ACS OMEGA
http://pubs.acs.org/journal/acsodf
Mini-Review

Open Access
This article is licensed under CC-BY-NC-ND 4.0

Recent Progress in Solar-Blind Photodetectors Based on Ultrawide Bandgap Semiconductors

Published as part of ACS Omega virtual special issue "At the Speed of Light: Recent Advances in Optoelectronics".

Lixia Wang, Shengming Xu, Jiangang Yang, Hui Huang, Zhe Huo, Jing Li, Xin Xu, Feng Ren, Yunbin He, Yaping Ma,* Weifeng Zhang,* and Xudong Xiao*

Cite This: ACS Omega 2024, 9, 25429−25447

Read Online

ACCESS | Metrics & More | Article Recommendations

ABSTRACT: Ultrawide bandgap (UWBG) semiconductors, including Ga_2O_3, diamond, $Al_xGa_{1-x}N$/AlN, featuring bandgaps greater than 4.4 eV, hold significant promise for solar-blind ultraviolet photodetection, with applications spanning in environmental monitoring, chemical/biological analysis, industrial processes, and military technologies. Over recent decades, substantial strides in synthesizing high-quality UWBG semiconductors have facilitated the development of diverse high-performance solar-blind photodetectors (SBPDs). This review comprehensively examines recent advancements in UWBG semiconductor-based SBPDs across various device architectures, encompassing photoconductors, metal−semiconductor-metal photodetectors, Schottky photodiodes, p-n (p-i-n) photodiodes, phototransistors, etc., with a systematic introduction and discussion of their operational principles. The current state of device performance for SBPDs employing these UWBG semiconductors is evaluated across different device configurations. Finally, this review outlines key challenges to be addressed, aiming to steer future research endeavors in this critical domain.

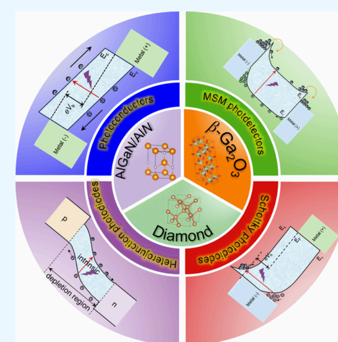

1. INTRODUCTION

In the invisible region of solar spectrum, ultraviolet (UV) radiation, constituting ~10% of the total solar energy, spans wavelength ranging from 10 to 400 nm. UV light is generally categorized into four subregions: extreme ultraviolet (EUV) spectrum (10−100 nm), ultraviolet C (UVC) spectrum (100−280 nm), ultraviolet B (UVB) spectrum (280−320 nm), and ultraviolet A (UVA) spectrum (320−400 nm) (Figure 1a). Prolonged exposure to UV radiation has been linked to genetic mutations and carcinogenic effects.[1] Fortunately, most UV radiation from sunlight can be absorbed by the stratospheric ozone layer and the earth's atmosphere. Notably, UV radiation with wavelength shorter than ~280 nm (UVC and EUV spectra) cannot penetrate the atmosphere and reach the earth's surface. The UV spectrum within the wavelength range of 200−280 nm is commonly referred to as solar-blind spectrum region (also called deep-UV, DUV). In the recent decades, spurred by rapid advancements of semiconductor industry, UV light detection, particularly solar-blind DUV photodetection, has garnered substantial interest due to the significant applications across diverse fields, including ozone-hole monitoring, chemical analysis, missile tracking, flame detection, arc detection, wireless communications, etc.[2]

Solar-blind photodetectors (SBPDs) were conventionally constructed by using low bandgap semiconductors, such as Si. However, photodetectors based on low bandgap semiconductors usually exhibit a broadband spectral response. Consequently, optical filters are necessitated for solar-blind detection, permitting the transmission of UV light while obstructing the visible portion of the solar spectrum.[3] Such filters incur both financial costs and operational limitations due to visible light leakage over time. As a result, attention has shifted toward wide bandgap (WBG) semiconductors with a bandgap surpassing traditional semiconductors (~3.1 eV) but smaller than that of insulators (~7 eV), for UV photodetection. WBG semiconductors, like SiC, GaN, GeS_2, and II−VI compounds (ZnO etc.), typically featuring bandgaps surpassing ~3.1 eV, exhibit rapid photoresponse speed and are blind to visible light (Figure 1b−e).[4] In addition, the high thermal conductivity of these WBG semiconductors permits operation in harsh environments (high temperature and high power). For the case of solar-blind optoelectronics, ultrawide bandgap (UWBG) semiconductors with a bandgap greater than 4.4 eV,

Received: March 26, 2024
Revised: May 17, 2024
Accepted: May 28, 2024
Published: June 5, 2024

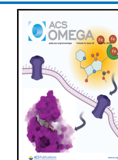

ACS Publications
© 2024 The Authors. Published by American Chemical Society

https://doi.org/10.1021/acsomega.4c02897
ACS Omega 2024, 9, 25429−25447

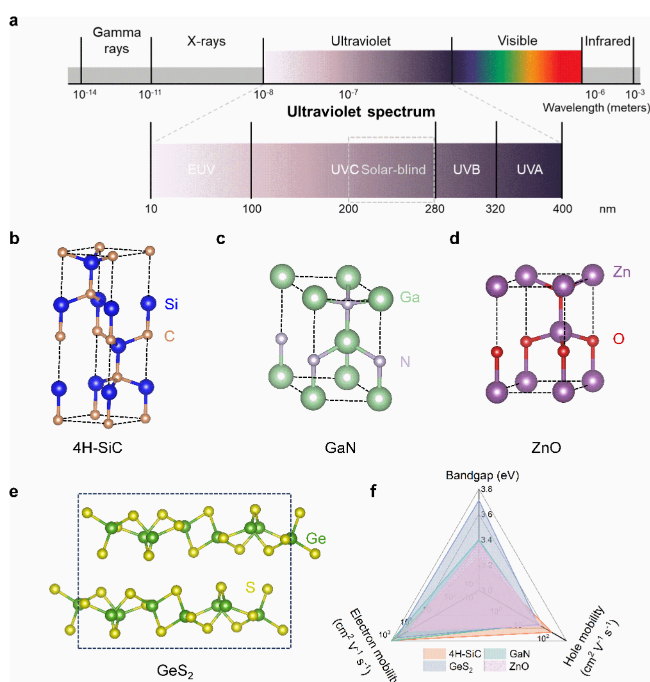

Figure 1. Ultraviolet radiation and wide bandgap semiconductors for photodetection. (a) UV spectral region and its subregions. (b−e) Crystal structures of WBG semiconductors, including (b) 4H-SiC, (c) GaN, (d) ZnO, and (e) GeS_2. The dash lines represent the unit cells. (f) Comparison of physical properties of WBG semiconductors.

corresponding to a wavelength below 280 nm, are particularly suitable. This category of materials includes Ga_2O_3, diamond, III-nitride compounds ($Al_xGa_{1-x}N$ and BN), and $Mg_xZn_{1-x}O$. In recent years, significant strides have been made in the development of high-performance SBPDs based on UWBG semiconductors. These detectors exhibit exceptional responsivity, high rejection ratios, rapid response speeds, and low noise.[5]

In this review, we present a comprehensive summary of the recent advancements on UWBG semiconductors for solar-blind photodetection. We first provide a brief introduction of prevalent device geometries utilized in contemporary SBPDs, detailing their working mechanisms, pros/cons, and key performance parameters. Subsequently, we systematically present and discuss the endeavors and notable advancements in diverse categories of SBPDs constructed from various UWBG semiconductors, focusing on Ga_2O_3, diamond, and $Al_xGa_{1-x}N$. At the end, we present open challenges and the future outlook to guide future research directions in this field.

2. BASICS OF PHOTODETECTOR

A photodetector is a device capable of converting an optical signal to an electrical one. Generally, the operation of the optoelectronic devices involves the following three processes (Figure 2): (i) generation of photoexcitons (electron−hole pairs) by incident light; (ii) separation and transport of photogenerated excitons; and (iii) charge carrier extraction at end electrodes to provide the output electrical signal.[6] The light absorption depends on the absorber properties, such as the bandgap, the absorption coefficient, and the thickness. The energy of the absorbed photons must be equal to or greater than the bandgap of the absorber material. For solar-blind optoelectronics, because of large absorption coefficient of DUV light, DUV light can be completely absorbed within a few micrometers of the material. Therefore, the absorber materials can adopt diverse configurations, including wafers, thin films, or nanostructures.

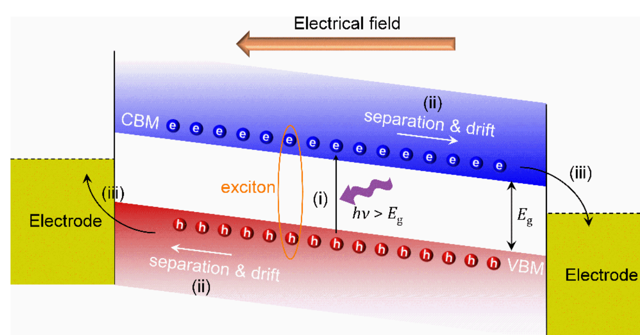

Figure 2. Illustration of the mechanism of photodetectors. The electric field can be induced by the built-in potential in the junction or the external bias supply.

2.1. Device Geometries.

In the currently reported SBPDs, diverse device architectures have been devised, including photoconductors, metal−semiconductor-metal (MSM) photodetectors, Schottky photodiodes, p-n (p-i-n) junction photodetectors, avalanche photodiodes (APD), and phototransistors.[7] In this section, we will discuss the working principles and pros/cons of these various device configurations.

2.1.1. Photoconductors.

The photoconductor device comprises a semiconductor layer as a channel with two ohmic contacts attached at both ends of the channel (Figure 3a, left panel). Photoconductors have attracted considerable attention for a long time due to their simple fabrication process, high responsivity, and low-cost merits. Its working principle hinges on the augmentation of conductivity owing to the generation of excess free carriers by photon absorption in the semiconductor (Figure 3a, right panel). Specifically, in the absence of light, the semiconductor hosts a low concentration of carriers, allowing only a small current (dark current, I_{dark}) to flow through the channel under an applied bias voltage. Upon illumination, the semiconductor absorbs photons with energy larger than its bandgap to generate electron−hole pairs, which are subsequently separated by the applied electric field. The resulting free electrons and holes migrate in opposite directions toward the electrodes, where they are collected.

The channel conductivity strongly depends on the intensity of incident light. Notably, the photocurrent (I_{ph}) is written as

$$I_{ph} = I_{light} - I_{dark} \quad (1)$$

where I_{light} is the channel current under illumination. The high dark current is detrimental to device performance. The photoconductive gain (G) is defined as the ratio of the number of photoexcited charge carriers collected by the electrodes to the number of photons absorbed in the semiconductor.

$$G = \frac{I_{ph}}{eP_{abs}/h\nu} = \frac{e(\mu_n\Delta n + \mu_p\Delta p)EA}{egV} = \frac{e(\mu_n\Delta n + \mu_p\Delta p)E}{egL} \quad (2)$$

where P_{abs}, $h\nu$, e, E, L, A, and V are the energy of absorbed photons per second, the photon energy, electronic charge, electric field intensity, channel length, the cross-sectional area of device, and the channel volume ($V = LA$), respectively, g is the carrier generation rate [equal to $P_{abs}/(h\nu V)$], μ_n and μ_p are the electron and hole mobility, respectively, Δn and Δp are the photogenerated electron and hole concentration, respectively.

https://doi.org/10.1021/acsomega.4c02897
ACS Omega 2024, 9, 25429−25447

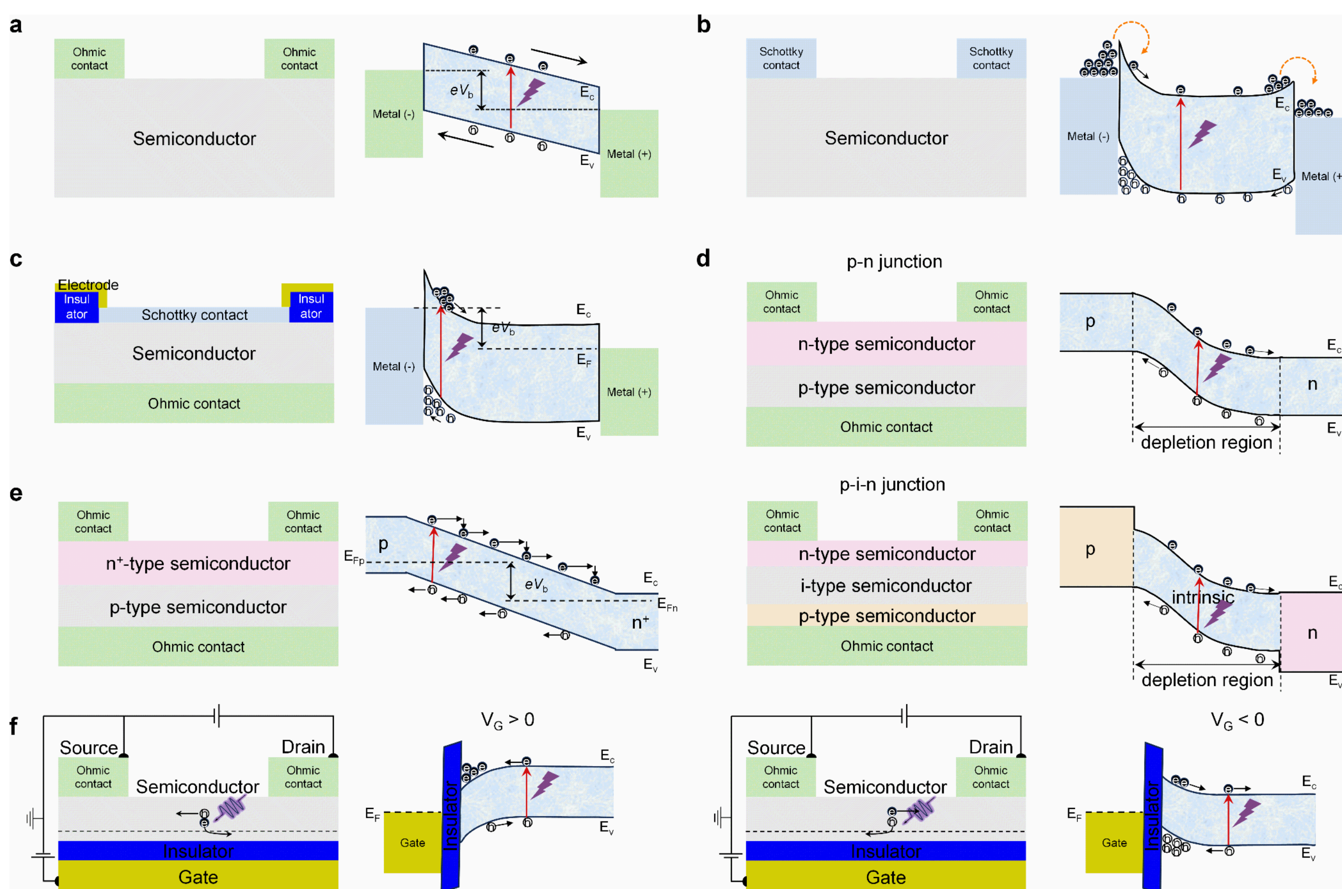

Figure 3. Various device geometries for photodetectors as well as their operational mechanisms. (a) A photoconductor has a conducting channel where the conductance changes with the incident light and ohmic contacts provide no barrier for photogenerated carriers. (b) An MSM photodetector is a planar device with two back-to-back Schottky contacts usually in an interdigitated configuration. (c) A Schottky photodiode employs a Schottky barrier at the metal−semiconductor interface to reduce the dark current. (d) A p-n junction photodiode offers a built-in potential to separate photogenerated carriers. A p-i-n junction photodetector has an intrinsic semiconducting layer that acts as the light absorber. The barriers between different doped regions cut back the diffusion of the carriers, thereby giving a fast response speed. (e) An avalanche photodiode has an electron accelerating region induced by a high external electric field. In this region, impact ionization occurs to provide the avalanche multiplication of photoexcited carriers. (f) A phototransistor can modulate the photo response by controlling the carrier density through a gate voltage.

In addition, $\Delta n = \Delta p$ as the excess carriers are generated in pairs. At steady state, the carrier generation rate must be equal to the recombination rate. Therefore,

$$\Delta n = g\tau_n \quad (3)$$

where τ_n is the lifetime of minority electrons in a semiconductor (assuming p-type semiconductor). By combining formula 2 and 3, we can get

$$G = \frac{\tau_n(\mu_n + \mu_p)E}{L} = \frac{\tau_n}{\tau_t}\left(1 + \frac{\mu_p}{\mu_n}\right) \quad (4)$$

where $\tau_t = L/(\mu_n E)$ is the transit time for the minority electrons to transport between two electrodes. A larger G can be achievable by a longer lifetime of minority carriers. Nevertheless, the response time, associated with the carrier recombination process, is further influenced by the lifetime of minority carriers. An increased G tends to prolong the response time. Thus, achieving a satisfactory overall performance necessitates striking a balance between G and response speed in a photoconductor. An undesirable drawback of photoconductors is the relatively high dark current. Nonetheless, due to the simple device architecture and ease of fabrication, photoconductors are useful for applications where fast response and low dark current are not necessities.

2.1.2. MSM Photodetectors. MSM photodetectors feature a straightforward device architecture akin to that of photoconductors, characterized by a low-doped semiconductor layer with two metallic contacts on the surface, forming two interconnected back-to-back Schottky barrier junctions (Figure 3b). To enhance the output current signals, the electrodes typically adopt an interdigitated configuration, offering a large photosensitive surface area while maintaining a short distance between the fingers. The operational mechanism mirrors that of photoconductors, where, in the absence of illumination, one Schottky junction is reverse-biased while the other is forward-biased due to the rectifying nature of the contacts, resulting in relatively low dark current compared to photoconductors. Under illumination, the presence of Schottky barriers necessitates a relatively high applied bias for effective separation and transport of photogenerated carriers. Due to the low junction capacitance of the planar geometry, MSM photodetectors generally exhibit fast response speeds. Additionally, MSM devices typically demonstrate high photoconductive gain, attributed to several factors. First, photoconductivity stems from long-lifetime traps of photocarriers at the semiconductor surface between the electrodes, inducing an asymmetric electric charge

https://doi.org/10.1021/acsomega.4c02897
ACS Omega 2024, 9, 25429−25447

distribution and facilitating additional carrier injection from the electrode via tunneling. Second, minority carriers may accumulate or become trapped near one electrode, leading to majority carrier injection from the other electrode through tunneling. Moreover, impact ionization under high electric fields contributes to photoconductive gain. However, MSM photodetectors typically exhibit relatively lower external quantum efficiency due to the electrode shadowing effect. This limitation can be mitigated by optimizing the width and pitch of electrode fingers and utilizing semitransparent electrodes. Overall, MSM photodetectors offer excellent performance, simple structure, and easy manufacturing, rendering them ideal for monolithic integration in optoelectronic circuits.

2.1.3. Schottky Photodiodes. The structure and fabrication of Schottky photodiodes are relatively simple, primarily relying on the Schottky junction formed at the metal−semiconductor interface, with the other metal−semiconductor contact serving as an ohmic contact (Figure 3c). These photodiodes can operate under zero bias thanks to the presence of built-in potential at the Schottky junction interface. The underlying principle involves that upon illumination with photon energy greater than the semiconductor bandgap, photon absorption occurs in the semiconductor, generating electron−hole pairs. These electron−hole pairs are either produced within the depletion region or migrate to it via diffusion, where they are subsequently separated by the built-in electric field. Furthermore, applying an appropriate reverse bias can reduce the dark current, augment the built-in electric field, and broaden the depletion region to enhance the photon absorption and the carrier separation, thereby promoting device performance. In comparison to photoconductors and MSM photodetectors, Schottky photodiodes offer several advantages, including high quantum efficiency, high signal-to-noise ratio, and rapid response speed.

2.1.4. p-n (p-i-n) Junction Photodetectors. The architectures of homo/heterojunction photodetectors are predominantly characterized by p-n and p-i-n junction structures. In p-n junction photodetectors, two semiconductors with opposite doping types are geometrically arranged (Figure 3d, upper panel). At the p-n junction interface, charge diffusion occurs to align their Fermi levels, leading to the formation of a depletion region (also called space charge region) and the creation of a built-in electric field. Eventually, the drift (induced by the built-in electric field) and the diffusion of carriers reach an equilibrium state. The operational principle relies on the photovoltaic effect, where photons with energy higher than the bandgap are absorbed by semiconductors, generating electron−hole pairs. These pairs diffuse from the junction to the depletion region within a diffusion length and are subsequently separated by the built-in electric field, causing photoexcited electrons and holes to move toward opposite electrodes. Such photodiodes can function under zero bias or reverse bias. Under zero bias, the relatively low dark current can improve specific detectivity (D^*) and sensitivity of the device. Under reverse bias, the expansion of the depletion region reduces carrier transit time and diode capacitance, thereby improving response speed. As a variant of p-n junctions, p-i-n photodiodes incorporate an intrinsic layer between p^+-type and n^+-type contact layers, with one layer typically being transparent (Figure 3d, bottom panel). In this case, the intrinsic layer facilitates light absorption. This configuration has garnered significant attention due to its potential for optimizing quantum efficiency (QE) and response speed through precisely controlling the thickness of depletion region.

p-n (p-i-n) photodiodes usually exhibit many advantages, including a low or zero working bias, a high input impedance, and a high working frequency. The fabrication process of p-n (p-i-n) photodiodes is notably intricate compared to photoconductors, MSM photodetectors, and Schottky photodiodes. It involves depositing semiconductor thin films with different doping types to construct the p-n (p-i-n) junctions. In particular, effective bipolar doping in UWBG semiconductors such as Ga_2O_3, diamond, and $Al_xGa_{1-x}N$ presents a bottleneck, necessitating the growth of various materials to form heterojunctions. Achieving precise control over growth processes is crucial for heterojunction epitaxy, ensuring high-quality interfaces and desired electronic properties. Considering factors such as lattice mismatch, strain, and doping profiles across the heterojunction interface, optimizing the epitaxy conditions to minimize defects, such as dislocations and stacking faults, plays an essential role in maintaining the integrity and functionality of the heterojunctions.

2.1.5. Avalanche Photodiodes. The APD devices typically exhibit structures similar to Schottky photodiodes or p-n (p-i-n) photodiodes (Figure 3e). The operational mechanism of APD primarily relies on the avalanche multiplication to provide internal current gain for the detection of low-density radiation. Under sufficiently high reverse bias, during the migration of photogenerated carriers to electrodes, electrons possess enough energy to initiate impact ionization, creating additional electron−hole pairs from the lattice. The number of created charge carriers will increase exponentially with distance. In general, APDs demonstrate fast response speed, high sensitivity to weak UV signals, and large current gain. However, the attainment of high gain often accompanies increased noise levels.

2.1.6. Phototransistors. The device configuration of phototransistors closely resembles that of conventional transistors, with the distinction that the channel region is left open for photon absorption (Figure 3f). The channel conductivity is tuned by the field effect through a gate electrode that is electrically isolated from the channel by a thin dielectric layer. By applying a gate voltage (V_G), the carrier density can be electronically controlled via field-effect modulation, thereby facilitating the suppression of dark current by operating the device in the depletion regime. The incident light creates photoexcited carriers to activate the channel conductance, leading to a photoconductive gain akin to the case of photoconductors. Compared to photodiodes, phototransistors typically demonstrate higher responsivity and sensitivity due to the increased photoconductive gain. However, they often exhibit slower response speeds than photodiodes.

2.2. Key Performance Parameters. In order to quantitatively compare the device performance of different photodetectors, several key performance parameters are used to evaluate the device characteristics as below:

(1) Cutoff wavelength (λ_0): The long wavelength limit of light the photodetector can detect. Usually measured in nanometers (nm).

$$\lambda_0 = \frac{hc}{E_g} \quad (5)$$

where E_g, h, and c are the bandgap of the absorber semiconductor, the Planck's constant, and the light speed, respectively.

https://doi.org/10.1021/acsomega.4c02897
ACS Omega 2024, 9, 25429−25447

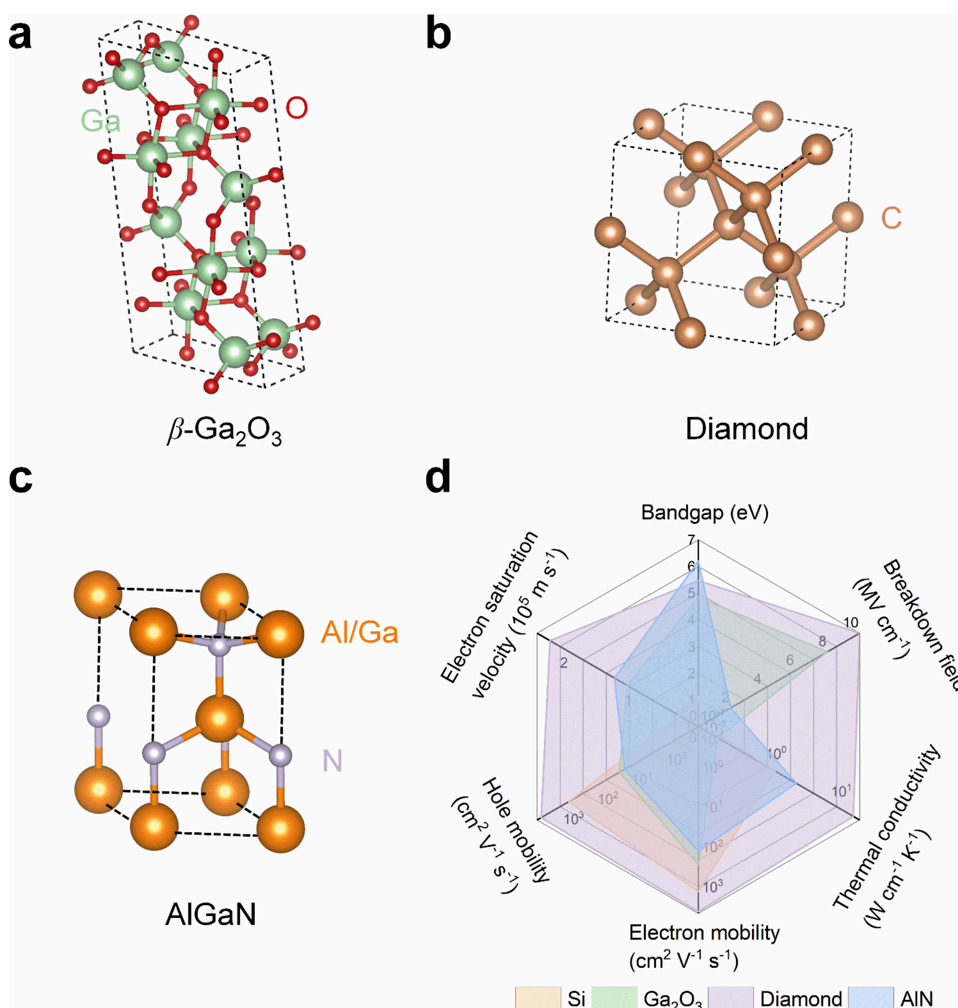

Figure 4. UWBG semiconductors and their physical properties. (a−c) Crystal structures of UWBG semiconductors, (a) β-Ga_2O_3, (b) diamond, and (c) AlGaN. The dashed lines represent the unit cells. (d) Comparison of physical properties of UWBG semiconductors.

(2) Dark current (I_{dark}): The residual current that flows in the photodetector without light irradiation, measured in Amperes.

(3) Photoresponsivity (R): The ratio of generated photocurrent to incident light power, is expressed by

$$R = \frac{I_{ph}}{P_{in}} = \frac{I_{light} - I_{dark}}{P_{in}} \tag{6}$$

where P_{in} is the incident light power. Measured in Amperes per Watt (A W^{-1}).

(4) Response time: The time it takes for the output to change in response to changes in the input light intensity. It is usually measured in two separate components, rise time (τ_r) and decay time (τ_d). Rise time and decay time are defined as the time taken for the photocurrent to increase from 10% to 90% and decrease from 90% of its peak to 10%, respectively. Alternatively, rise time and decay time can be extracted by fitting the time-resolved photocurrent curves.

(5) Noise-equivalent power (NEP): The minimum incident light power required to achieve a signal-to-noise ratio of unity at a bandwidth of 1 Hz. Measured in Watts per square root Hertz (W $Hz^{-1/2}$).

$$NEP = \frac{I_n}{R} \tag{7}$$

where I_n is the current noise in Amperes per square root Hertz (A $Hz^{-1/2}$).

(6) Specific detectivity (D^*): The figure-of-merit of detection sensitivity for photodetectors, i.e., how well a weak signal can be detected compared to the detector noise. D^* is determined by

$$D^* = \frac{\sqrt{A_{eff}}R}{\sqrt{2eI_{dark}}} \tag{8}$$

where A_{eff} is the effective device area under illumination. It is usually measured in Jones (cm $Hz^{1/2}$ W^{-1}). Alternatively, it is proportional to the reciprocal of NEP, expressed as

$$D^* = \frac{\sqrt{A_{eff}\Delta f}}{NEP} \tag{9}$$

where Δf is the bandwidth.

(7) Quantum efficiency (QE): Ability of the photodetector to convert the input light signal to an output signal, containing two subcomponents, the internal and external quantum efficiency (IQE/EQE). EQE represents the ratio of the number of the charge carriers with

https://doi.org/10.1021/acsomega.4c02897
ACS Omega 2024, 9, 25429−25447

contributing to photocurrent to the number of incident photons, whereas IQE is the ratio of the number of the charge carriers collected to the number of absorbed photons. QE is measured in terms of percentages. Generally, EQE is the preferred figure-of-merit in photodetectors which can be measured directly and is determined by

$$\mathrm{EQE} = \frac{hcR}{e\lambda} \tag{10}$$

where λ is the wavelength of incident light.

Among these, photoresponsivity, response time, and specific detectivity are generally considered as the most important performance parameters.

3. MATERIALS

3.1. Ga_2O_3. Gallium oxide (Ga_2O_3) has recently emerged as a promising candidate for the applications in solar-blind photodetectors and high-power electronic devices. Due to its diverse crystal structures, Ga_2O_3 is found in five polymorphs: rhombohedral (α), monoclinic (β), defective spinel (γ), cubic (δ), and hexagonal (ε) phases.[8] Among these, β-Ga_2O_3 stands out as the most stable structure, with a formation energy ranking of $\beta > \varepsilon > \alpha > \delta > \gamma$. This phase can be thermally converted from other metastable-phase Ga_2O_3 structures within a temperature range of 300 to 870 °C.[8d] Notably, owing to its exceptional chemical and thermal stability, β-Ga_2O_3 has garnered significant interest for applications in high-temperature and harsh environments. The β-Ga_2O_3 structure exhibits a monoclinic crystal arrangement under the $C2/m$ space group, with lattice parameters of a = 12.21 Å, b = 3.04 Å, c = 5.80 Å, and β = 103.8° (Figure 4a).[8e] Within the β-Ga_2O_3 unit cell, there are two crystallographically distinct Ga cations, situated at distorted tetrahedral and octahedral coordination, alongside three distinct O anions, comprising two types of 3-fold coordination and one type of 4-fold coordination. This unique structural arrangement engenders anisotropic physical properties, including optical, thermal, and electrical characteristics.[9] The growth of β-Ga_2O_3 bulk crystals commonly employs methods such as edge-defined film-fed growth (EFG), Czochralski (CZ), float zone (FZ), and Bridgman methods, whereas β-Ga_2O_3 films and nanostructures can be synthesized through techniques including sputtering, hydride vapor phase epitaxy (HVPE), metal−organic chemical vapor deposition (MOCVD), molecular beam epitaxy (MBE), pulsed laser deposition (PLD), and atomic layer deposition (ALD).[10]

3.2. Diamond. Diamond, as a metastable allotrope of graphene, constitutes a solid crystal where each carbon atom forms tetrahedral covalent bonds with four neighboring carbon atoms, resulting in a face-centered cubic crystal structure with a lattice constant of a = 3.57 Å under $Fd\bar{3}m$ space group (Figure 4b). Renown for its high carrier mobility, exceptional thermal conductivity, low thermal coefficient of expansion, an ultrawide bandgap, and chemical inertness, diamond boasts numerous applications at the forefront of technology, particularly in quantum sensing, solar-blind photodetection, DUV light-emitting diodes (LEDs), and power electronics.[11] The diamond bulk crystals are commonly grown by high-pressure-high-temperature method (HPHT) while chemical vapor deposition (CVD) methods are typically utilized for the deposition of diamond thin films.[12]

3.3. AlGaN/AlN. $Al_xGa_{1-x}N$ (AlGaN) alloy, a III-nitride compound, exists in the hexagonal wurtzite crystal structure under $P6_3mc$ space group (Figure 4c). By adjusting the Al composition from 0 to 1, the lattice constants vary from a = 3.19 Å, c = 5.19 Å to a = 3.11 Å, c = 4.98 Å, simultaneously altering the direct bandgap from 3.4 to 6.2 eV.[13] When the Al content (x) is larger than 0.4, the cutoff wavelength becomes smaller than 280 nm, suitable for solar-blind photodetection. Moreover, these materials exhibit high electron mobility, saturation velocity, high breakdown field, large absorption coefficient, and good thermal stability and conductivity, endowing them suitable for applications in high-power and high-speed electronics, blue/UV LEDs, and UV/DUV photodetectors.[14] AlGaN films can be synthesized using various techniques, including direct nitridation, carbothermic, physical vapor transfer (PVT), CVD, MBE, sputtering, and PLD methods.[15]

Among the trio of UWBG semiconducting materials discussed, diamond emerges as the standout candidate, boasting superior electron and hole mobilities, exceptional thermal conductivity, and an ideal bandgap of ∼5.5 eV (Figure 4d). These attributes empower diamond for DUV photodetection with rapid response even in demanding environmental conditions. Nonetheless, due to the low carrier concentration of intrinsic diamond, it exhibits insulating properties with a resistivity exceeding 10^{16} Ω cm, thereby necessitating efficient doping. At present, boron can be introduced into diamond to effectively realize p-type doping, while n-type doping remains challenging due to the difficult incorporation of atoms (P etc.) larger than carbon into the closely packed and rigid diamond lattice. In addition, the unavailability of large-area, single-crystal diamond poses a challenge for demonstrating device concepts effectively. For AlGaN/AlN, tunable bandgaps over a wide range by adjusting the Al content enable optimization for specific photodetection wavelengths. Moreover, the relatively high thermal stability makes it suitable for high-temperature operation and harsh environments. However, there are still some shortcomings or challenges for AlGaN/AlN in solar-blind photodetection: (i) The commercial unavailability of large-area AlGaN/AlN single-crystal substrates limits the device applications. (ii) High-quality epitaxy of AlGaN thin films remains challenging due to the presence of high-density of defects and cracks. (iii) Due to the high activation energy of acceptors, effective p-type doping of AlGaN thin films is difficult to realize. In contrast, significant progress has been made in the development of large-area (4 in. or above), high-quality single-crystal β-Ga_2O_3 substrates for epitaxy, with multiple commercial suppliers such as Novel Crystal Technology, Inc. However, β-Ga_2O_3 faces two main drawbacks for device applications: (i) The low thermal conductivity, potentially undermining its applications in high-temperature conditions. (ii) The absence of efficient p-type doping, hampering the fabrication of p-n homojunction devices.

4. GA_2O_3-BASED PHOTODETECTORS

4.1. Photoconductors. Photoconductors based on β-Ga_2O_3 have garnered considerable attention owing to their straightforward device architecture. Typically, β-Ga_2O_3 thin films are grown on sapphire substrates for device fabrication.[16] Notably, the Schottky barriers between UWBG semiconductors and metallic electrodes are not easily diminished to achieve reliable ohmic contact. The commonly used electrode materials include Au, Al/Ti, Ti/Au, Ni/Au, and Cr/Au. Kokubun et al. successfully prepared β-Ga_2O_3 thin film on sapphire substrate by sol−gel method for solar-blind photodetection with a cutoff wavelength of 270 nm.[16a] However, the low quality of the β-

Ga_2O_3 thin film limited the photoresponsivity to 8×10^{-5} A W^{-1}. Oshima et al. employed plasma-assisted MBE to grow β-Ga_2O_3 thin film containing α-Ga_2O_3 and rotational domains, achieving a photoresponsivity of 0.037 A W^{-1} and a quantum efficiency of 18%.[16b] In addition, Hu et al. designed a β-Ga_2O_3 photodetector with interdigitated electrodes on a sapphire substrate by MOCVD.[16c] Owing to the avalanche multiplication by the large electric field underneath the gold electrodes, the photoresponsivity of the photodetector reaches 17 A W^{-1}, corresponding to a quantum efficiency of 8228% under a bias voltage of 20 V. To improve the quality of β-Ga_2O_3 by reducing the scattering or/and trapped centers of photoexcited carriers, Zhang et al. introduced N_2O as reaction gas to grow thin film.[16d] Consequently, the resulting SBPD exhibits a high photoresponsivity of 26.1 A W^{-1}, a large ratio of photocurrent to dark current (PDCR), and fast response speed (τ_r = 0.48 s and τ_d = 0.18 s). Moreover, a β-Ga_2O_3 homoself-templated buffer layer was preintroduced for the growth of β-Ga_2O_3 thin film by MBE, leading to an improvement in the crystalline quality of β-Ga_2O_3 thin film.[16e] As a result, a photodetector with a small dark current of 0.04 nA, a high PDCR of 10^4, a large photoresponsivity of 259 A W^{-1}, and a high EQE of 7.9×10^4 % was realized under a bias of 20 V. The high quantum efficiency is possibly ascribed to the avalanche multiplication.

Furthermore, a high concentration of the intrinsic oxygen vacancies (V_O) in Ga_2O_3 thin film typically hampers the photodetection performance, resulting in a large dark current, low specific detectivity, and tardy response speed. Photodetectors often exhibit high photoresponsivity, but with the persistent photoconductivity (PPC) effect due to the capture of minority carriers on V_O defects, leading to slow response speed. Postannealing under an oxygen atmosphere and element doping are commonly employed to mitigate the effect of V_O defects on the photodetection performance.[17] The postannealing treatment under an oxygen atmosphere can significantly decrease the concentration of V_O defects, suppressing the dark current (visible light response) to enhance the PDCR (out-of-band rejection ratio).[17a] Additionally, reducing the concentration of oxygen vacancies can realize the transition of metal−semiconductor contact from ohmic to Schottky to reduce the response time.[17b] Zinc doping is also effective in decreasing the concentration of oxygen vacancies to improve the photodetection performance, such as low dark current, high PDCR, and fast response speed.[17e−g] By combing the Zn doping and postannealing methods, the device exhibits a peak photoresponsivity of 210 A W^{-1} at 232 nm and an out-of-band rejection ratio ($R_{232\ nm}/R_{320\ nm}$) of 5×10^4, which are five times and three times higher, respectively, than the parameters of as-grown β-Ga_2O_3 photodetector.[17f]

Despite Ga_2O_3 thin films, low-dimensional Ga_2O_3 nanostructures, such as nanowires (NWs), nanobelts (NBs), nanoribbons (NRBs), nanodots (NDs), and nanosheets, have been explored for SBPD fabrication.[18] Compared to the photodetectors of Ga_2O_3 thin films, those based on Ga_2O_3 nanostructures generally exhibit lower dark current, larger PDCR, and faster response speed. For instance, Li et al. developed an efficient bridging method to assemble β-Ga_2O_3 NWs into SBPDs, demonstrating a high 250-to-280 nm rejection ratio ($\sim 2 \times 10^3$), low photocurrent fluctuation, and a ultrafast decay time ($\ll$ 20 ms).[18a] Moreover, the device based on multilayer (l00) facet-oriented β-Ga_2O_3 NRBs exhibits an ultralow dark current (<10^{-14} A), a high photoresponsivity (851 A W^{1-}), and a fast response speed (<0.3 s).[18b] Feng et al. successfully synthesized two-dimensional β-Ga_2O_3 nanosheets by directly oxidizing few-layer GaSe in air. The photodetector based on β-Ga_2O_3 nanosheets shows a fast and stable photosensitivity to 254 nm light with a decent photoresponsivity of 3.3 A W^{-1}, a high detectivity of 4.0×10^{12} Jones, and a large EQE of 1600%.[18c] Li et al. synthesized Ga_2O_3 NBs and investigated the dependence of the photoresponse parameters of the device on the light intensity, the environment and the nanobelt size.[18d] With the increase of light intensity, the photocurrent increases, while quantum efficiency remains almost unchanged at ∼180%. The quantum efficiency exceeding 100% is governed by hole traps. Once the light intensity increases to the critical intensity, the number of available hole-traps will decrease, leading to the saturation and even decrease of the quantum efficiency due to the increasing chance of recombination of photogenerated electron−hole pairs. Additionally, Tian et al. reported a photodetector based on In-doped Ga_2O_3 nanobelts, exhibiting a higher photoresponsivity, a higher quantum efficiency (2.72×10^5%), and a faster response speed than that of the undoped device.[18g] The excellent performance of the device may be attributed to the chemically pure, high-quality single crystals, the large surface-to-volume ratio, short channel length, and low recombination barrier. Very recently, Zhou et al. synthesized Sn-doped β-Ga_2O_3 microbelts (MBs) to fabricate SBPD arrays with superior photodetection performance, including a dark current of 0.5 pA, response time of 38.8 μs, a PDCR of 10^8, and a photoresponsivity of 300 A W^{-1}.[18f]

4.2. MSM Photodetectors. Compared to the photoconductor architecture, the metal−semiconductor interfaces in MSM photodetectors present Schottky barriers that benefit photodetection performance by reducing dark current and enhancing response speed.[19] Typically, reducing the concentration of oxygen vacancies in β-Ga_2O_3 can increase the Schottky barrier. By delicately controlling the oxygen flux during the growth process, the concentration of oxygen vacancies can be effectively reduced to suppress the deep-level defects and increase the Schottky barrier.[19a,b] Additionally, nitrogen doping can also decrease the concentration of V_O in Ga_2O_3 thin films.[19c] Recently, the insertion of a graphene monolayer in a W Schottky contact can induce the reduction of the interfacial state density and the strong suppression of metal Fermi-level pinning, resulting in an ideal Schottky barrier height (0.53 eV), thereby promoting the performance with a high photoresponsivity (14.49 A W^{-1}), a high EQE (7044%), and a fast response speed (τ_r = 0.139 s and τ_d = 0.2 s).[19g]

The performance of Ga_2O_3 MSM photodetectors can be improved by controlling the growth temperature, annealing, and growing seed layer (SL).[20] For example, the β-Ga_2O_3 thin films prepared by low-cost sol−gel method at the annealing temperature of 700 °C has a high RCDR and fast response speed.[20b] Moreover, Chen et al. grew a single-crystal β-Ga_2O_3 nanoparticle SL, suppressing the deep-level defects and increasing the Schottky barrier, to improve the photodetection performance.[20c] Intriguingly, the SBPD of β-Ga_2O_3 thin film fabricated on a cost-effective Si substrate using a high-temperature SL-assisted method can operate in a self-powered mode, attributed to differing Schottky barrier heights at two ends.[20d] Transparent optoelectronics are pivotal for next generation “see-through” electronic and optoelectronic devices, facilitating integration with transparent components, such as transparent memories, display panels, and batteries. To realize transparent SBPDs, transparent conductive electrodes, such as indium zinc oxide (IZO), indium tin oxide (ITO), and

https://doi.org/10.1021/acsomega.4c02897
ACS Omega 2024, 9, 25429−25447

graphene, are used instead of traditional metal electrodes.[21] Zhang et al. developed a fully transparent MSM-architecture Ga_2O_3 SBPD with embedded ITO electrodes, demonstrating an excellent performance with an ultralow dark current (1.6 pA), a high UV-to-visible rejection ratio (1.3×10^{12}), a large photoresponsivity (74.9 A W^{-1}), and a high specific detectivity of (7.4×10^{15} Jones) at a bias of 10 V.[21a] In addition, the integration of exfoliated β-Ga_2O_3 microlayers with graphene yields MSM-structure SBPDs with a high responsivity (~29.8 A W^{-1}), a high PDCR (~1×10^4), and a high detectivity (~1×10^{12} Jones).[21b]

4.3. Schottky Photodiodes. Analogous to the MSM architecture, dissimilar contact configurations are employed in β-Ga_2O_3 Schottky photodiodes, comprising one Schottky contact and one ohmic contact at opposing ends. The fabrication typically involves the use of Ti/Au electrodes for achieving ohmic contact, while Schottky junctions with Ga_2O_3 are formed using Au, Pt, Ni/Au, and two-dimensional (2D) materials.[22] Generally, vertically stacked devices incorporate a transparent metal layer (<10 nm) at the Schottky side. Oshima et al. prepared Ni/Au and Ti/Au electrodes to establish Schottky and ohmic contacts on two surfaces of a (100)-orientated β-Ga_2O_3 substrate (thickness: 400 μm), respectively.[22a] The resulting photodetector demonstrates substantial photoresponsivity of 2.6−8.7 A W^{-1} at the wavelengths of 200−260 nm, coupled with a high PDCR of higher than 10^6. Armstrong et al. employed deep-level optical spectroscopy characterization to reveal the roles of self-trapped holes (STHs) in the high photoconductive gain.[22b] The accumulation of STHs above the valence band of Ga_2O_3 is spatially localized near Schottky contact, leading to a reduction of the Schottky barrier and a significant increase in reverse leakage current, thus contributing to a large photoconductive gain. Similarly, Peng et al. devised a self-powered SBPD based on a Pt/β-Ga_2O_3 Schottky barrier diode, delivering a notable PDCR of 1×10^4, and rapid response speed (τ_r = 65 ms and τ_d = 15 ms) at zero bias.[22c] Moreover, leveraging a 2D/3D graphene/$PtSe_2$/β-Ga_2O_3 Schottky junction, the device achieves a high responsivity of 76.2 mA W^{-1}, a large PDCR of ~10^5, a remarkable specific detectivity of ~10^{13} Jones, and ultrashort response time of 12 μs.[22d] Furthermore, Xu et al. realized a fast-speed and self-powered Au (5 nm)/β-Ga_2O_3 vertical Schottky SBPD with a large detection area (7×7 mm^2), showcasing a peak photoresponsivity of 9.78 A W^{-1} and a corresponding specific detectivity of 3.29×10^{14} Jones at 212 nm, and shortest response time of <5 μs in self-powered operational mode.[22e] On the basis of a laterally planar Ti/Ga_2O_3/Au device geometry with interdigitated electrodes, the Schottky photodetector can operate in avalanche mode at a reverse bias of 60 V, exhibiting a high responsivity of 9780.23 A W^{-1}, an ultrahigh PDCR of 1.88×10^7, a high specific detectivity of 9.48×10^{14} Jones, and a high EQE of 4.77×10^6%.[22f] Overall, in Ga_2O_3-based devices employing MSM structures or Schottky photodiodes, the substantial photocurrent gain and elevated quantum efficiency are frequently attributed to the presence of STHs, which serve to reduce the Schottky barrier height, or alternatively, to avalanche multiplication facilitated by impact ionization.[23]

4.4. p-n (p-i-n) Junction Photodetectors. β-Ga_2O_3 is an intrinsically n-type UWBG semiconductor since the oxygen vacancies act as shallow donor centers. At present, successful p-type conductivity in β-Ga_2O_3 has not been achieved by doping with Mg, Zn, etc., usually acting as deep acceptors, due to the almost flat valence band maximum, inducing high effective mass of holes.[9e,24] The quest for suitable p-type semiconducting substrates that are combined with β-Ga_2O_3 to form p-n junctions is crucial for SBPDs with minimal dark current and ultrafast response speed. Various materials, including SiC, Si, ZnO, Nb:$SrTiO_3$, NiO, Cu_2O, GaN, SnO_2, and graphene, have been explored for their potential to form p-n junctions with β-Ga_2O_3. In fact, the majority of the above p-n junction photodiodes can only work under bias voltage.[7e,25] For example, Nakagomi et al. demonstrated a β-Ga_2O_3 layer on a 6H-SiC substrate, yielding a β-Ga_2O_3/6H-SiC heterostructure photodiode sensitive to 260 nm ultraviolet light with millisecond-level response time under reverse bias.[25a] Based on graphene/β-Ga_2O_3 heterojunction, the reported device by Kong et al. demonstrates a large photoresponsivity of 39.3 A W^{-1}, and a high specific detectivity of 5.92×10^{13} Jones under a bias of 20 V.[25b] In addition, the SBPD based on SnO_2/β-Ga_2O_3 heterojunction can operate in an avalanche mode with excellent photodetection performance at 254 nm.[25m]

Up to now, zero-power-consumption Ga_2O_3-based p-n heterojunction SBPDs have been realized.[26] Highly crystallized β-Ga_2O_3 is important for fabricating high-performance self-powered SBPDs. Guo et al. developed a SBPD device based on a β-Ga_2O_3/Nb: $SrTiO_3$ heterojunction for the first time, enabling self-powered solar-blind detection with a low photoresponsivity of 2.6 mA W^{-1}, and a relatively fast response speed in the order of tens of milliseconds.[26e] Zhao et al. developed a ZnO-Ga_2O_3 core−shell heterostructure microwire for solar-blind photodetection, showing a low responsivity of 9.7 mA W^{-1}, a high UV/visible rejection ratio of 6.9×10^2, and short response time in submillisecond under zero bias.[26g] To further promote the performance of self-powered photodetectors, doping β-Ga_2O_3 with Sn, Ta etc., is an effective approach for enhancing the built-in electric field in p-n heterojunction and improving the conductivity of β-Ga_2O_3. By depositing a Sn-doped n-type Ga_2O_3 thin film onto a p-type GaN thick film, the SBPD based on a GaN/Sn:Ga_2O_3 p−n junction exhibits a low dark current of 18 pA, a large photoresponsivity of 3.05 A W^{-1} (254 nm), a high PDCR of ~10^4, an ideal detectivity of 1.69×10^{13} Jones, and a short response time of 18 ms under zero bias.[7d] In addition, Chen et al. grew a β-Ga_2O_3 thin film with a Ta doping concentration of 0.23 at. % on a porous p-type GaN substrate, yielding a high photoresponsivity (1.88 A W^{-1}), a high PDCR (2.3×10^3), a high detectivity (2.7×10^{13} Jones), and a short rise/decay time (0.15/0.14 s) under 222 nm light illumination.[26f]

Moreover, the construction of a p-i-n junction can increase the SCR width, facilitating the separation and transport of photogenerated carriers.[27] Chen et al. developed a p-GaN/i-Ga_2O_3/n-Ga_2O_3 heterojunction for solar-blind detection (248 nm), showcasing a decent responsivity (72 mA W^{-1}), a PDCR (18 800), a high specific detectivity (3.22×10^{12} Jones), and a fast response speed (τ_r = 7 ms and τ_d = 19 ms), without an external power supply.[27a] Recently, a p-i-n heterojunction SBPD based on a Ta doped n-Ga_2O_3/i-Ga_2O_3/p-GaN structure demonstrates an excellent photodetection performance under 222 nm UV light illumination, including a high photoresponsivity of 8.67 A W^{-1}, a high detectivity of 1.08×10^{14} Jones, and short rise/decay time (86/50 ms).[27c] Additionally, Kan et al. fabricated p-graphene/γ-Ga_2O_3 NDs/n-SiC photodetectors, demonstrating a decent performance with 250 nm light illumination under zero bias.[27b]

https://doi.org/10.1021/acsomega.4c02897
ACS Omega 2024, 9, 25429−25447

5. DIAMOND-BASED PHOTODETECTORS

5.1. Photoconductors. Because of the absence of high doping levels for diamond and large Schottky barriers between diamond and most metal electrodes, it remains challenging to obtain low-resistance ohmic contacts at the metal−diamond junction. Currently, several electrodes, such as Au, Ti/Au, Ti/TiN, and Ti/tungsten carbide (WC), have been reported to obtain ohmic contacts to diamond. For planar diamond-based SBPDs, interdigitated geometry of electrodes is commonly adopted for the collection of photogenerated carriers.[28] Yu et al. presented a UV photodetector based on CVD-grown polycrystalline diamond thin film, demonstrating a photoresponsivity of 0.63 A W^{-1}.[28a] Moreover, based on a homoepitaxially grown diamond thin film with unintentional boron doping, the planar photoconductor exhibits a low dark current of around 1 pA, and a large photoresponsivity of 6 A W^{-1} at 220 nm under a bias of 3 V.[28b] Instead of metal electrodes, Lin et al. used a laser-induced graphitization method to prepare graphite electrodes on a single-crystalline diamond wafer, forming an ohmic contact with diamond.[28c] Under a bias of 50 V, the device exhibits a peak photoresponsivity of 21.8 A W^{-1}, a large detectivity of 1.39×10^{12} Jones, and a large rejection ratio of $\sim 10^4$ at 218 nm. In addition, Qiu et al. constructed 8 × 8 planar pixels with Ti/Au electrodes on high-quality single crystal diamond for high-performance photodetection with a low dark current (0.1−1 pA), a high PDCR (10^5), a high photoresponsivity (22.6 A W^{-1}), a decent detectivity (4.2×10^{14} Jones), and a short response time (13 ns) at 222 nm under a bias of 50 V.[28d]

In addition, the construction of 3D electrodes is beneficial for further enhancing carrier collection efficiency. Generally, the 3D electrodes in diamond bulk can be fabricated through laser writing, ion beam lithography, and down-top methods.[12e,29] Alemanno et al. used laser-induced graphitization to fabricate graphite electrodes with diamond to form ohmic contacts for nuclear radiation detection.[29a] Liu et al. reported the fabrication of UV photodetector with 3D tungsten electrodes, revealing a high responsivity of 9.94 A W^{-1} with a rejection ratio of 10^3 at 220 nm under a bias of 5 V.[12e] Notably, groove-shaped Ti/Au electrodes are also designed for a diamond UV detector, leading to 50% enhancement of photoresponsivity in DUV range compared to planar structure device.[29b]

5.2. MSM Photodetectors. To date, numerous MSM diamond-based SBPDs have been explored by using Ti/Au, Al, Au, Pd, and WC as electrode materials, forming Schottky contacts with diamond.[30] Binari et al. compared the device performance of MSM photodetectors based on natural, synthetic, and polycrystalline insulating diamonds, discovering that natural diamond demonstrated the highest quantum efficiency of 39% and the highest UV/visible response ratio of 10^3 at 200 nm.[30a] The poor performance of synthetic diamond is ascribed to the low-quality polycrystalline diamond crystals and high impurity performance concentrations. With the development of microwave plasma CVD (MPCVD) technique, Wang et al. fabricated an MSM SBPD on a high-quality MPCVD-deposited diamond thin film, demonstrating a high photoresponsivity of 16.2 A W^{-1} corresponding to a high EQE of 92% at 220 nm under a bias of 6 V.[30b] Nonetheless, the rise/decay time is extended to 6/23 min, due to the trapping effect of shallow levels. In addition, the reduction in electrode spacing can enable the full depletion of the spacing at a low bias, thereby significantly enhancing DUV photoresponsivity.[30c,d]

Localized surface plasmon (LSP) method can also provide opportunities for further improving the performance of SBPDs.[11g,31] By precisely tuning the size of Pd nanoparticles (NPs), the diamond SBPD with 40 nm NPs exhibits the highest photoresponsivity and UV/visible rejection ratio, 3250 and 34 times larger than that of pure diamond photodetectors, respectively.[31a] In addition, Shi et al. developed an LSP-enhanced MSM SBPD by assembly of Al crescent-shaped arrays on boron-doped homoepitaxial diamond thin films, demonstrating over 10-fold higher photoresponsivity than bare diamond detector at 225 nm under a bias of 5 V.[31b] Interestingly, Zhou et al. fabricated a high-performance nanoplasmonic 1D diamond UV photodetector by integrating boron-doped ultrananocrystalline diamond (UNCD) nanowires with Pt NPs, showing an ultrahigh photoresponsivity of 388 A W^{-1}, a short response time of 20 ms, and a decent UV/visible rejection ratio of 10^5 in a self-powered operation mode.[11g]

The introduction of hydrogen plasma surface treatment can modulate the Schottky barrier at metal/diamond interfaces and surface defect states of diamond, leading to the enhancement of photodetection performance.[32] Due to the traps of photoexcited electrons by surface defect states and the reduction of Schottky barrier height, the SBPD device at 220 nm under a bias of 13 V exhibits a fast photoresponse (0.16 μs) with an ultrahigh photoresponsivity of 524.9 A W^{-1}, and a detectivity of 3.42×10^{15} Jones, which are the highest values among the reported diamond-based SBPDs.[32a] By controlling the voltage of Al top gate ($V_G = -1.5$ V) on a hydrogen-terminated diamond, the phototransistor can work under an ultralow bias of 10 mV with high performance (R and D^* are 146.7 A W^{-1} and 6.19×10^{11} Jones, respectively) at 213 nm.[32b]

5.3. Schottky Photodiodes. Many materials, such as Ag, Al, Au, Ru, WC etc., have been utilized to construct Schottky photodiodes.[33] In 1996, Whitfield et al. reported planar diamond photodiodes with gold Schottky and Ti/Ag/Au ohmic contacts shows a sharp cutoff in photoresponse in DUV with low dark currents under reverse biases.[33a,b] To realize thermally stable Schottky contacts with diamond, Koide compared the rectifying characteristics of the metal contacts, such as Ti, Mo, Cr, Pd, Co, WC, and hafnium nitride (HfN), revealing that the Schottky electrode materials should not react with diamond at elevated temperatures.[33c,d] The resulting photodetectors exhibit a high DUV/visible rejection ratio of 10^6 at a reverse bias of 2 V. In addition, the diamond-based photodiode using WC Schottky contact can operate in self-powered mode, achieving a DUV (210 nm)/visible rejection ratio of 10^5 at zero bias.[33e] To date, self-powered Schottky photodiodes based on diamond have rarely been reported. Li et al. used a spin-coated Ag NW network on a single-crystal diamond to form a self-powered Schottky photodiode, displaying a relatively high photocurrent (200 pA) at zero bias.[33f] Girolami et al. introduced an asymmetric contact geometry with both Al/Au electrodes deposited on the two surfaces of a diamond plate to fabricate a vertically structured diamond-based SBPD, showing a photoresponsivity of 0.19 mA W^{-1}, and a detectivity of 1.91×10^{11} Jones at 225 nm under zero bias.[33g] Recently, Liu et al. constructed self-powered SBPDs based on vertical Ru/diamond Schottky diodes. The resulting Semi and Mesh photodetectors exhibit low dark currents of 0.53 and 0.007 pA, relatively high photoresponsivities of 10.3 and 16.2 mA W^{-1}, high detectivities of 3.8×10^{12} and 5.2×10^{13} Jones, respectively at 220 nm under zero bias.[33h]

https://doi.org/10.1021/acsomega.4c02897
ACS Omega 2024, 9, 25429−25447

5.4. p-n (p-i-n) Junction Photodetectors. n-type doping of diamond is essential to achieve diamond-based p-n (p-i-n) homojunctions. To date, effective doping by P or S element has been reported to achieve n-type doped diamond.[11i,34] In 2001, Koizumi et al. successfully constructed a UV light-emitting diode based on a diamond p-n junction with P-doped (n-type) and B-doped (p-type) diamond layers.[11i] p-i-n diamond-based SBPDs fabricated with B-doped, undoped, and P-doped diamond layers has relatively high photoresponsivity of 10−30 mA W^{-1} around 200 nm.[34d,e]

Although all-diamond based p-n (p-i-n) homojunctions have been successfully established, the device performance of these SBPDs is mainly limited by the poor quality of n-type diamond. Therefore, heterojunction photodetectors have attracted extensive attention, by combing diamond with other materials, such as ZnO, TiO_2, NiO, Ga_2O_3, and graphene.[11f,35] ZnO materials possess notable advantages including a high exciton binding energy (60 meV), excellent optical quality, and favorable piezoelectric properties. However, the rapid recombination of electron−hole pairs limits their application in UV photodetectors. To enhance UV detection performance, ZnO nanorods (NRs) were integrated with boron-doped diamond to form heterojunction photodetectors. The device displayed a high PDCR of 143, with rise and decay times of 4.9 and 6.4 s, respectively, at 365 nm under a reverse bias of 1 V.[35a] Similarly, Su et al. deposited ZnO films with different thicknesses on diamond substrates to construct a heterojunction, and ZnO film with thickness of 100 nm on a diamond substrate displayed a high photoresponsivity of 308 A W^{-1} at 270 nm under a bias of 30 V.[35b] TiO_2, another wide bandgap semiconductor, can be combined with diamond to enhance response and broaden the spectral detection range. Liu et al. deposited TiO_2 (thickness: 450 nm) onto a diamond epitaxial layer and observed that the device displayed an obvious photoresponse selectivity between UV and visible light with the rejection ratio of $\sim 10^2$.[35c] Additionally, ultrathin TiO_2/diamond UV photodetectors with various thicknesses of TiO_2 showed that thinner TiO_2 films absorb less UV light, leading to improved response performance.[35d] To improve the quality of heterojunction between graphene and diamond, Wei et al. transferred graphene onto the smooth backside of peeled-off microcrystalline diamond to construct a vertically structured photodetector, exhibiting high responsivity and gain factor.[35e] Via in situ KrF excimer, Li et al. transformed sp^3 diamond to sp^2 graphite, developing an all-carbon DUV detector with a diamond/graphite structure. This detector demonstrated a high photoresponsivity of 15 mA W^{-1} and a short response time of 86 μs at 220 nm under a bias of 5 V.[35f]

6. ALGAN/ALN-BASED PHOTODETECTORS

6.1. Photoconductors/MSM Photodetectors. Ti/Au or Ti/Al/Ti/Au electrodes are usually used for the formation of ohmic contacts with AlGaN/AlN, whereas other materials often form Schottky contacts with AlGaN/AlN.[36] In 2004, Lebedev et al. constructed a solar-blind $Al_{0.51}Ga_{0.49}N$ photoconductor with an $Al_{0.67}Ga_{0.33}N$ integrated filter, obtaining a high solar-blind response with a narrow wavelength range.[36a] The device exhibits a peak photoresponsivity of ∼0.2 A W^{-1} and short response time of ∼30 ms at 258 nm under 5 V bias.[36b] Moreover, Nikishin et al. introduced AlN/GaN period superlattices to reduce the density of inversion domains (IDs) in AlN layers. The photodetector with ID density of 10^6 cm^{-2} exhibits an ultralow dark current of 50 fA under a bias of 30 V, and a peak photoresponsivity of 0.08 A W^{-1} at ∼202 nm under a bias of −10 V.[36c]

An AlGaN MSM SBPD based on high temperature AlN epitaxy fabricated by Xie et al. shows an ultralow dark current (fA).[36d] Localized surface plasmon and 3D electrodes also were adopted to further improve the performance of MSM structured AlGaN photodetectors. Bao et al. constructed an AlGaN-based SBPD using Al NPs, displaying a peak photoresponsivity of 0.288 A W^{-1} at 288 nm under a bias of 5 V, two times higher than that without Al NPs, due to the localized surface plasmon resonance effect of Al NPs.[36e] Chen et al. fabricated an AlGaN MSM photodetector with low-temperature AlN cap layer and inductively coupled plasma recessed 3D electrodes, demonstrating an ultralow dark current of 1.12 pA, a peak photoresponsivity of 0.129 A W^{-1}, and a large PDCR of 6.4×10^4 at 320 nm under a bias of 5 V.[36f] In addition, an AlN spacer layer was introduced into a AlGaN-based SBPD between the high-Al barrier layer and the low-Al channel layer to suppress the dark current as well as to improve response. The device exhibits a low dark current of <1 pA, a PDCR of $>10^8$ at 205 nm, and a peak photoresponsivity of 1.2×10^6 A W^{-1} at 234 nm under a bias of 5 V.[36g]

On the basis of MSM device geometry, AlGaN phototransistors have attracted extensive attention recently.[37] In 2021, Zhang et al. demonstrated a high-performance solar-blind phototransistor based on AlGaN/GaN high-electron mobility transistor (HEMT) configuration.[37a] The device exhibits a high responsivity of 3.6×10^7 A W^{-1}, a large EQE of 1.7×10^8%, and a detectivity of 6.5×10^{18} Jones at 265 nm under the gate-source and drain-source voltages of −8.2 and 8 V, respectively. Moreover, Lu et al. constructed a solar-blind phototransistor based on a quasi-pseudomorphic AlGaN heterostructure, showing a superhigh photoresponsivity of 2.9×10^9 A W^{-1}, a record high detectivity of 4.5×10^{21} Jones, and an ultrafast response speed at the nanosecond level under the illumination of 213 nm light.[37b] By introducing double 2D electron gas channels, a UV photodetector based on an AlGaN/GaN double-channel HEMT exhibits a high photoresponsivity of 2.1×10^7 A W^{-1}, and a high specific detectivity of 1.7×10^{15} Jones at 360 nm.[37c]

6.2. Schottky Photodiodes. The structure of Schottky photodiodes consists of two asymmetric contacts with a Schottky contact and an ohmic contact.[38] In 2008, Osinsky et al. first reported an AlGaN Schottky UV photodiode with Pd metals for Schottky contact and Ti/Al/Ti/Au electrodes for ohmic contact, which exhibits a peak photoresponsivity of 70 mA W^{-1} at 290 nm under zero bias.[38a] In addition, a lateral geometry Schottky photodiode composed of In−Si-codoped AlGaN with Pd Schottky contact has a peak responsivity of 33 mA W^{-1}, and a large rejection ratio (R_{275}/R_{305}) of $>10^3$ at 275 nm under zero bias.[38b] With a transparent indium−tin-oxide Schottky contact, the AlGaN SBPD exhibits a low dark current of <1 pA (20 V), a peak photoresponsivity of 44 mA W^{-1} (a reverse bias of 50 V), and short rise time of 13 ps.[38c] Recently, Gu et al. reported a self-powered AlGaN-based MSM SBPD with one side of metal/semiconductor Schottky contact.[38d] When operated under zero bias, the device presents an ultralow dark current of 0.78 pA, a high peak photoresponsivity of 40 mA W^{-1}, and a corresponding detectivity of 3.1×10^{12} Jones at ∼275 nm. Guo et al. realized a self-powered MSM solar-blind AlGaN photodetector by in-plane polarization modulation, exhibiting a peak photoresponsivity of 0.2 A W^{-1} at 230 nm under zero bias, and a PDCR of over 10^5.[38e]

https://doi.org/10.1021/acsomega.4c02897
ACS Omega 2024, 9, 25429−25447

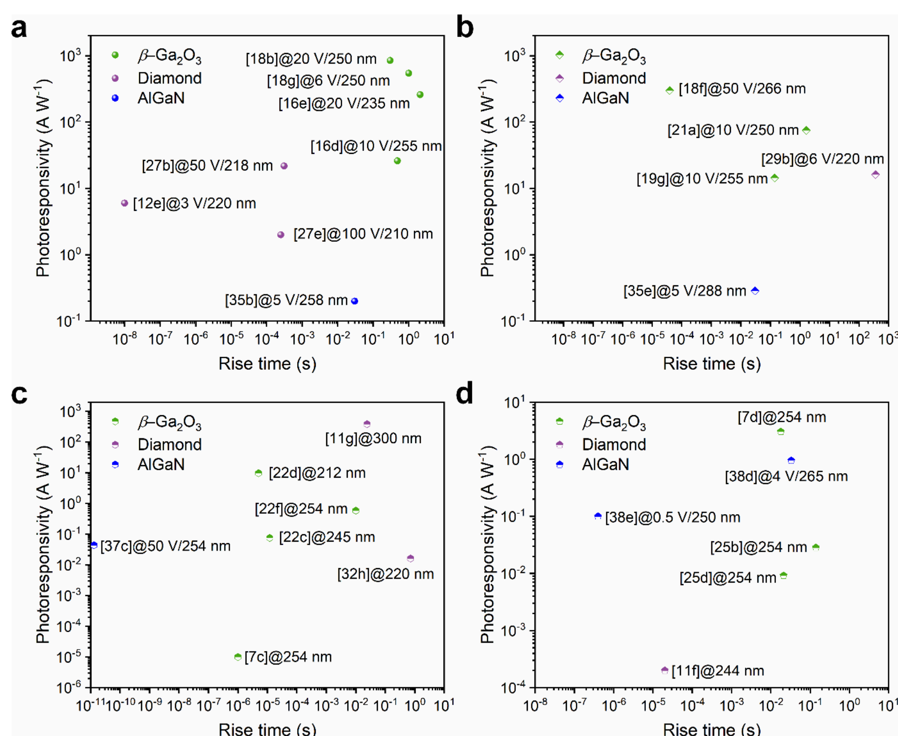

Figure 5. Performance comparison of the current scenario in UWBG semiconductor based SBPDs with various device configurations, (a) photoconductors, (b) MSM photodetectors, (c) Schottky photodiodes, and (d) p-n (p-i-n) junction photodetectors. The data point without a bias in (c) and (d) represents the performance parameters of the device operated in self-powered mode.

6.3. p-n (p-i-n) Junction Photodetectors. Unlike the p-n junction, the thickness of the i-type layer in p-i-n junction is important due to the trade-off between light absorption and response speed. So far, AlGaN based p-i-n junction SBPDs have been extensively investigated.[39] In 1999, an AlGaN-based p-i-n SBPD on laterally epitaxial GaN template shows a low dark current density of 10 nA cm^{-2}, and a peak photoresponsivity of 50 mA W^{-1} at 285 nm under a reverse bias of 5 V.[39a] In 2004, McClintock et al. reported an AlGaN-based back-illuminated p-i-n SBPD with a peak photoresponsivity of 136 mA W^{1-} at 282 nm without bias.[39b] Through optimization, they fabricated an AlGaN SBPD array on sapphire substrate, demonstrating a peak photoresponsivity of ∼176 mA W^{-1}, and a large EQE of ∼80% at 275 nm under zero bias.[39c] Interestingly, an SBPD based on quantum-disk NWs with p-i-n AlGaN heterostructures by introducing surface passivation exhibits a low dark current of 6.22 nA, a large photoresponsivity of 0.95 A W^{-1}, and a decent detectivity of 6.4×10^{11} Jones at 265 nm under a bias of −4 V.[39d]

7. PERFORMANCE COMPARISON OF SBPDS BASED ON VARIOUS UWBG SEMICONDUCTORS WITH IDENTICAL DEVICE GEOMETRY

Due to their appealing properties, inorganic UWBG semiconductors, including Ga_2O_3, diamond, and AlGaN/AlN, have provided ideal platforms for solar-blind photodetection. On the basis of them, various device geometries, i.e., photoconductors, MSM photodetectors, Schottky photodiodes, p-n (p-i-n) junction photodetectors, avalanche photodiodes, and phototransistors, have been extensively investigated and employed. At present, the reported SBPDs can typically attain decent photoresponse performance in terms of low dark current, high photoresponsivity, large PDCR, and rapid response speed. Figure 5 compares the performance parameters (photoresponsivity versus rise time) of representative SBPDs based on UWBG semiconductors in various device configurations. Obviously, β-Ga_2O_3 SBPDs have been explored much more extensively and usually exhibit the highest photoresponsivity values accompanying with short response time, while AlGaN/AlN-based devices normally suffer from low photoresponsivity. In particular, AlGaN/AlN SBPDs based on Schottky photodiodes/p-n (p-i-n) junctions remain at a low level in response performance, usually requiring external bias supplies. SBPDs made from diamond display moderate performance. The superior optoelectronic performance of β-Ga_2O_3-based SBPDs can be attributed to several factors. First, β-Ga_2O_3 has been subject to thorough study and optimization, resulting in high-quality material with minimal defect density. Additionally, the availability of high-quality substrates and well-established fabrication processes contribute to the exceptional performance of β-Ga_2O_3-based SBPDs. Despite its excellent material properties, diamond-based SBPDs may exhibit moderate performance due to challenges in doping and heterojunction formation, which can introduce defects and degrade device performance. AlGaN/AlN-based devices often encounter higher defect densities, stemming from the significant lattice mismatch between AlGaN/AlN and substrates such as sapphire. Meanwhile, the high-temperature epitaxy process of AlGaN/AlN can induce stress due to the large thermal expansion mismatch with substrates, leading to the formation of dislocations. Moreover, SBPDs based on micro/nanostructures of UWBG semiconductors often exhibit better photoresponse performance than those based on their thin film counterpart. Compared with commercial UV-enhanced Si photodetectors, SBPDs based on UWBG semiconductor usually show comparable or higher photoresponsivity and specific detectivity values. However, the response speed of these devices is difficult to match that of

https://doi.org/10.1021/acsomega.4c02897
ACS Omega 2024, 9, 25429−25447

commercial detectors. However, SBPDs based on UWBG semiconductors can operate at high temperatures and in harsh environment. This merit paves the way for realizing highly sensitive solar-blind photodetection in many practical applications, where traditional Si-based DUV photodetectors can scarcely be applicable. Due to issues such as device reproducibility and reliability, SBPDs based on UWBG semiconductors can complement rather than replace Si photodetectors at the current stage.

8. SUMMARY AND FUTURE OUTLOOK

Despite notable achievements, several challenges must be addressed prior to the commercialization of UWBG semiconductor-based SBPDs (Figure 6a). In the case of β-Ga_2O_3, considerable progress has been achieved in bulk crystal growth, epitaxial deposition, doping control, etc., providing a robust foundation for developing high-performance SBPDs. However, p-type doping of β-Ga_2O_3 remains elusive, owing to the high activation energy of acceptors and strong localization of holes when simply doped with Mg, Zn, etc. In addition, a huge trade-off exists between photoresponsivity and response time. These two parameters are usually competing because trap states in β-Ga_2O_3 can enhance photoconductive gain but slow response speed induced by their prolonged lifetime. For diamond, a key challenge is the limited size of commercially available diamond substrates, which falls short of the requirements of the semiconductor industry. Moreover, the quality of grown polycrystalline diamonds is insufficient to date. However, it is crucial to establish strategies for the realization of n-type doped diamond, which poses a great challenge for applying diamond in p-n (p-i-n) and Schottky junction photodetectors. In the case of AlGaN/AlN, large-area AlGaN/AlN single-crystal substrates are not readily available commercially. Growth of AlGaN thin films on bulk AlGaN/AlN single-crystal substrates can alleviate severe lattice mismatches encountered when using sapphire substrates. Additionally, achieving high-quality epitaxy of high-Al-content AlGaN alloys is challenging due to the presence of defects and cracks during deposition. Effective p-type doping of AlGaN thin films is also problematic due to the high activation energy of Mg dopants in high-Al-content AlGaN and resulting crystal quality issues. Nanostructured UWBG semiconductors are garnering increasing research interest for solar-blind photodetection due to their cost-effectiveness and scalability. Nonetheless, as the heterogeneity of nanostructured materials can significantly impact the homogeneity of device performance, it is crucial yet challenging to reliably control not only the diameter, length, crystallinity, and orientation assembly of these materials, but also the physical and chemical properties of these materials.

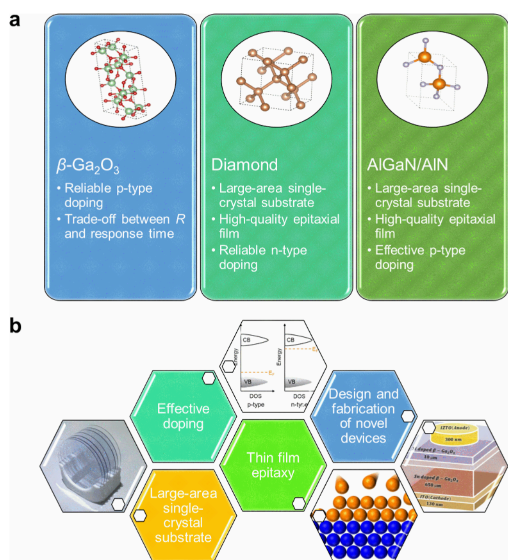

Figure 6. Future challenges and research directions. (a) The faced challenges in SBPDs based on various UWBG semiconductors. (b) Future research directions in the UWBG semiconductor-based SBPDs.

In spite of many obstacles in this field, there is much room for the development of SBPDs based on UWBG semiconductors. The future research will focus primarily on production of high-quality UWBG semiconductors by growing single crystals and depositing thin films, realization of effective n- and p-type doing of these materials, and design and fabrication of novel device structures (Figure 6b). In addition, to promote the commercialization of UWBG-semiconductor based SBPDs, several important future research directions are discussed below:

(i) High-quality single crystals and thin films of UWBG semiconductors. The availability of large-area, high-quality single-crystal substrates is crucial for the fabrication of devices based on UWBG semiconductors. Homoepitaxy on such substrates offers a promising avenue for reducing defect density by leveraging lattice matching. Additionally, achieving high-quality epitaxy of thin films is pivotal for advancing the field of SBPDs based on UWBG semiconductors. Reliable thin film epitaxy methods ensure repeatability, reproducibility, and long-term stability, thereby enhancing the performance and durability of UWBG-semiconductor-based SBPDs. Expanding the availability of high-quality single crystals and thin films of UWBG semiconductors will further drive innovation and development in this field.

(ii) Effective bipolar doping strategies. Since the advent of semiconductors, precise doping with shallow donors and acceptors has represented the pivotal step required to transition semiconductor materials from scientific curiosity to technological significance. Realizing efficient bipolar doping (both p-type and n-type) in UWBG semiconductors holds paramount importance for the development of p-n (p-i-n) homojunction-based solar-blind photodetection devices. Homoepitaxial growth of UWBG semiconductors with different doping types can effectively reduce defect densities by circumventing lattice mismatch issues compared to heteroepitaxial growth. At present, challenges persist in achieving p-type doping in β-Ga_2O_3, n-type doping in diamond, and p-type doping in AlGaN, necessitating substantial research endeavors to overcome these hurdles.

(iii) Large-scale production and integration. In light of the anticipated advancements in the fabrication of large-area (wafer-scale) substrates and thin films of UWBG semiconductors in the foreseeable future, there arises a pressing need to develop environmentally sustainable and economically viable processing methodologies to enable large-scale production and integration. Such advancements are crucial for the realization of practical applications, particularly in the realm of solar-blind imaging, where the integration of individual components, such as pixel devices, into focal plane arrays (FPAs) holds immense promise. Leveraging existing mature semi-

https://doi.org/10.1021/acsomega.4c02897
ACS Omega 2024, 9, 25429−25447

conductor processes in tandem with these advancements offers a pathway to scale up production while mitigating adverse environmental impacts and streamlining manufacturing costs. Leveraging existing mature semiconductor processes in tandem with these advancements offers a pathway to scale up production while minimizing adverse environmental impacts and reducing manufacturing costs.

(iv) Introduction of novel concepts. Some novel concepts hold promise for enhancing device performance, reducing power consumption, or catering to specific application scenarios. Localized surface plasmonic effects offer a pathway to further enhance the performance of SBPDs. Exploring phenomena such as the photovoltaic effect, piezophototronic effect, thermophototronic effect, and photogating effect holds promise for improving device functionality and achieving self-powered operation. The next generation of "see-through" electronic and optoelectronic technologies enables the seamless integration of these devices into transparent or semitransparent substrates. This integration allows users to simultaneously access digital information or images while seeing through the device. Transparent solar-blind photodetectors find applications in smart glasses or wearable devices for outdoor activities, facilitating real-time monitoring and protection against UV radiation. In automotive contexts, these detectors can enhance safety by detecting UV signals from sunlight or oncoming vehicles without obstructing the driver's view. Moreover, in aerospace and defense sectors, transparent solar-blind photodetectors serve surveillance, reconnaissance, and target acquisition purposes, offering valuable information while maintaining transparency for unobstructed viewing.

(v) Exploration of new UWBG semiconductors. While AlGaN/AlN, diamond, and Ga_2O_3 are the UWBG materials that have garnered significant interest in recent years, it is important to note that all UWBG materials are relatively immature, with numerous others warranting exploration. For instance, materials such as $Zn_xMg_{1-x}O$, $MgGa_2O_4$, Al_2O_3, and II−IV−N compounds like $ZnSiN_2$ and $MgSiN_2$, as well as various 2D materials such as h-BN, hold promise for further investigation. In practical terms, the selection of DUV sensing materials should align closely with the requirements of target applications, considering the significant variability in performance exhibited by UWBG semiconductor SBPDs across different metrics. Furthermore, the compatibility between materials and fabrication processes, as well as operational conditions, should be carefully considered when choosing photosensitive materials. It is anticipated that continued advancements in the field of UWBG semiconductor-based solar-blind photodetection will address the substantial demands across various applications in the future.

AUTHOR INFORMATION

Corresponding Authors

Yaping Ma − *School of Future Technology, Henan Key Laboratory of Quantum Materials and Quantum Energy, Henan University, Zhengzhou 450046, P. R. China; School of Physical Science and Technology and Key Laboratory of Artificial Micro- and Nano-Structures of Ministry of Education, Wuhan University, Wuhan 430072, P. R. China; Institute of Quantum Materials and Physics, Henan Academy of Sciences, Zhengzhou 450046, P. R. China;* orcid.org/0000-0003-3907-6881; Email: mustc@henu.edu.cn

Weifeng Zhang − *School of Future Technology, Henan Key Laboratory of Quantum Materials and Quantum Energy, Henan University, Zhengzhou 450046, P. R. China; Institute of Quantum Materials and Physics, Henan Academy of Sciences, Zhengzhou 450046, P. R. China*; Email: wfzhang6@163.com

Xudong Xiao − *School of Future Technology, Henan Key Laboratory of Quantum Materials and Quantum Energy, Henan University, Zhengzhou 450046, P. R. China*; Email: xdxiao@whu.edu.cn

Authors

Lixia Wang − *School of Future Technology, Henan Key Laboratory of Quantum Materials and Quantum Energy, Henan University, Zhengzhou 450046, P. R. China; School of Physical Science and Technology and Key Laboratory of Artificial Micro- and Nano-Structures of Ministry of Education, Wuhan University, Wuhan 430072, P. R. China*

Shengming Xu − *School of Future Technology, Henan Key Laboratory of Quantum Materials and Quantum Energy, Henan University, Zhengzhou 450046, P. R. China*

Jiangang Yang − *School of Physical Science and Technology and Key Laboratory of Artificial Micro- and Nano-Structures of Ministry of Education, Wuhan University, Wuhan 430072, P. R. China*

Hui Huang − *School of Materials Science & Engineering, Hubei University, Wuhan 430062, P. R. China; School of Physical Science and Technology and Key Laboratory of Artificial Micro- and Nano-Structures of Ministry of Education, Wuhan University, Wuhan 430072, P. R. China*

Zhe Huo − *School of Future Technology, Henan Key Laboratory of Quantum Materials and Quantum Energy, Henan University, Zhengzhou 450046, P. R. China; Key Laboratory of Bio-inspired Smart Interfacial Science and Technology of Ministry of Education, School of Chemistry, Beihang University, Beijing 100191, P. R. China*

Jing Li − *Key Laboratory of Bio-inspired Smart Interfacial Science and Technology of Ministry of Education, School of Chemistry, Beihang University, Beijing 100191, P. R. China;* orcid.org/0000-0002-5627-4153

Xin Xu − *State Key Lab of Optoelectronic Materials and Technologies, Guangdong Province Key Laboratory of Display Material and Technology and School of Electronics and Information Technology, Sun Yat-sen University, Guangzhou 510275, P. R. China; School of Physical Science and Technology and Key Laboratory of Artificial Micro- and Nano-Structures of Ministry of Education, Wuhan University, Wuhan 430072, P. R. China*

Feng Ren − *School of Physical Science and Technology and Key Laboratory of Artificial Micro- and Nano-Structures of Ministry of Education, Wuhan University, Wuhan 430072, P. R. China;* orcid.org/0000-0002-9557-5995

Yunbin He − *School of Materials Science & Engineering, Hubei University, Wuhan 430062, P. R. China;* orcid.org/0000-0002-7179-4392

Complete contact information is available at: https://pubs.acs.org/10.1021/acsomega.4c02897

Notes

The authors declare no competing financial interest.

https://doi.org/10.1021/acsomega.4c02897
ACS Omega 2024, 9, 25429−25447

Biographies

Lixia Wang received a B.S. degree in optoelectronic information science and engineering from Bengbu University. She is currently a Master student in photoelectric information engineering at Henan University. Her research interests include epitaxial growth of ultrawide bandgap semiconductor Ga_2O_3, and scanning tunneling microscopy (STM) surface physics.

Shengming Xu is now a Master student at Henan University. His research focuses on surface growth and surface physics.

Jiangang Yang is a PhD candidate at the School of Physical Science and Technology of Wuhan University. His research interests focus on the growth and characterization of two-dimensional materials.

Hui Huang obtained a Bachelor of Engineering degree from Hubei University in 2022. Currently, he is a Master student at Hubei University. He is mainly conducting research on various physical properties of thin-layer gallium oxide materials using STM, LEED, XPS and other means.

Zhe Huo is now a Master student at Henan University. Her research interests focus on the exfoliation of two-dimensional materials and its applications.

Jing Li is a professor at Beihang University. He received his Ph.D. in physical chemistry from University of Chinese Academy of Sciences in 2016. His research interests include the preparation, intercalation, and surface modification of two-dimensional materials.

Xin Xu is currently a PhD student in Electronic Science and Technology at Sun Yat-sen University. His research interests include low-dimensional materials, thin-film solar cells, and electrocatalysis.

Feng Ren is a professor at Wuhan University. He received his Ph.D. from Wuhan University in 2006. His research interests include ion beam modification of materials, surface plasmon of metal nanostructures, and radiation tolerance nanomaterials.

Yunbin He is a professor at Hubei University. He received his Ph.D. in solid physics from Justus Liebig University Giessen in 2003. His research interests include wide bandgap semiconductor films and their ultraviolet electronics/optoelectronics, functional oxide materials and their photoelectric conversion/energy applications, design, and preparation of low-dimensional nanomaterials and exploration of new devices.

Yaping Ma is a professor, and Yellow River Scholar at Henan University. He received his Ph.D. in materials science and engineering from the Chinese University of Hong Kong in 2017. His research interests focus on the growth and physical properties of low-dimensional materials and topological materials, and electronic/optoelectronic devices.

Weifeng Zhang is a professor at Henan University. He received his Ph.D. in condensed matter physics from Nanjing University in 2003. His research interests include low-dimensional quantum materials and topological catalysis.

Xudong Xiao is a professor at Wuhan University. He received his Ph.D. in physics from University of California, Berkeley in 1992. His research interests include surface science, CIGS solar cells, perovskite solar cells, and tandem solar cells.

■ ACKNOWLEDGMENTS

Y.M. acknowledges the support from Natural Science Foundation of Henan Province (Grant No. 242300420627) and Start-up Foundation of Henan University (Grant No. CX3050A0960147). X.X. and F.R. acknowledge the financial support from Major Program of Hubei Province (Grant No. 2023BAA009).

■ REFERENCES

(1) Kneissl, M.; Seong, T.-Y.; Han, J.; Amano, H. The emergence and prospects of deep-ultraviolet light-emitting diode technologies. *Nat. Photonics* **2019**, *13* (4), 233−244.

(2) (a) Liao, M.; Koide, Y.; Alvarez, J.; Imura, M.; Kleider, J.-P. Persistent positive and transient absolute negative photoconductivity observed in diamond photodetectors. *Phys. Rev. B* **2008**, *78* (4), No. 045112. (b) Pearton, S.; Yang, J.; Cary, P. H.; Ren, F.; Kim, J.; Tadjer, M. J.; Mastro, M. A. A review of Ga_2O_3 materials, processing, and devices. *Appl. Phys. Rev.* **2018**, *5* (1), No. 011301. (c) Razeghi, M. III-nitride optoelectronic devices: from ultraviolet toward terahertz. *IEEE Photonics J.* **2011**, *3* (2), 263−267. (d) Oshima, T.; Okuno, T.; Arai, N.; Suzuki, N.; Hino, H.; Fujita, S. Flame detection by a β-Ga_2O_3-based sensor. *Jpn. J. Appl. Phys.* **2009**, *48* (1R), No. 011605.

(3) (a) Wood, R. Remarkable optical properties of the alkali metals. *Phys. Rev.* **1933**, *44* (5), 353. (b) Mu, J.; Lin, P.-T.; Zhang, L.; Michel, J.; Kimerling, L.; Jaworski, F.; Agarwal, A. Design and fabrication of a high transmissivity metal-dielectric ultraviolet band-pass filter. *Appl. Phys. Lett.* **2013**, *102* (21), 213105.

(4) (a) Pant, R.; Singh, D. K.; Chowdhury, A. M.; Roul, B.; Nanda, K. K.; Krupanidhi, S. B. Highly responsive, self-powered a-GaN based UV-A photodetectors driven by unintentional asymmetrical electrodes. *ACS Appl. Electron. Mater.* **2020**, *2* (3), 769−779. (b) Yang, Y.; Liu, S. C.; Wang, X.; Li, Z.; Zhang, Y.; Zhang, G.; Xue, D. J.; Hu, J. S. Polarization-sensitive ultraviolet photodetection of anisotropic 2D GeS_2. *Adv. Funct. Mater.* **2019**, *29* (16), 1900411. (c) Krishnamurthi, V.; Ahmed, T.; Mohiuddin, M.; Zavabeti, A.; Pillai, N.; McConville, C. F.; Mahmood, N.; Walia, S. A Visible-Blind Photodetector and Artificial Optoelectronic Synapse Using Liquid-Metal Exfoliated ZnO Nanosheets. *Adv. Opt. Mater.* **2021**, *9* (16), 2100449. (d) Wang, K.; Wang, H.; Chen, C.; Li, W.; Wang, L.; Hu, F.; Gao, F.; Yang, W.; Wang, Z.; Chen, S. High-Performance Ultraviolet Photodetector Based on Single-Crystal Integrated Self-Supporting 4H-SiC Nanohole Arrays. *ACS Appl. Mater. Interfaces* **2023**, *15* (19), 23457−23469. (e) Li, Z.; Yan, T.; Fang, X. Low-dimensional wide-bandgap semiconductors for UV photodetectors. *Nat. Rev. Mater.* **2023**, *8* (9), 587−603. (f) Wang, X.; Tan, J.; Han, C.; Wang, J.-J.; Lu, L.; Du, H.; Jia, C.-L.; Deringer, V. L.; Zhou, J.; Zhang, W. Sub-angstrom characterization of the structural origin for high in-plane anisotropy in 2D GeS_2. *ACS Nano* **2020**, *14* (4), 4456−4462. (g) Chen, S.; Cao, B.; Wang, W.; Tang, X.; Zheng, Y.; Chai, J.; Kong, D.; Chen, L.; Zhang, S.; Li, G. Large-scale m-GeS_2 grown on GaN for self-powered ultrafast UV photodetection. *Appl. Phys. Lett.* **2022**, *120* (11), 111101.

(5) (a) Cheng, L.; Wu, Y.; Cai, W.; Zheng, W. Diamond immersion photodetector for 213 nm deep-ultraviolet photodetection. *Mater. Today Phys.* **2023**, *36*, 101164. (b) Zheng, W.; Huang, F.; Zheng, R.; Wu, H. Low-dimensional structure vacuum-ultraviolet-sensitive ($\lambda <$ 200 nm) photodetector with fast-response speed based on high-quality AlN micro/nanowire. *Adv. Mater.* **2015**, *27* (26), 3921−3927. (c) Cai, Q.; You, H.; Guo, H.; Wang, J.; Liu, B.; Xie, Z.; Chen, D.; Lu, H.; Zheng, Y.; Zhang, R. Progress on AlGaN-based solar-blind ultraviolet photodetectors and focal plane arrays. *Light-Sci. Appl.* **2021**, *10* (1), 94. (d) Chen, Y.; Lu, Y.; Liao, M.; Tian, Y.; Liu, Q.; Gao, C.; Yang, X.; Shan, C. 3D solar-blind Ga_2O_3 photodetector array realized via origami method. *Adv. Funct. Mater.* **2019**, *29* (50), 1906040. (e) Zheng, Q.; Huang, F.; Ding, K.; Huang, J.; Chen, D.; Zhan, Z.; Lin, Z. MgZnO-based metal-semiconductor-metal solar-blind photodetectors on ZnO substrates. *Appl. Phys. Lett.* **2011**, *98* (22), 221112. (f) Kalra, A.; Muazzam, U. U.; Muralidharan, R.; Raghavan, S.; Nath, D. N. The road ahead for ultrawide bandgap solar-blind UV photodetectors. *J. Appl. Phys.* **2022**, *131* (15), 150901. (g) Shen, L.; Zhang, T.; Liu, Y.; Wu, H.; Wang, F.; Pan, X.; Ye, Z. Research progress in solar-blind UV detectors based on wide-band semiconductor Ga_2O_3. *J. Mater. Eng.* **2023**, *51* (10), 13−26.

(6) Sze, S. M.; Ng, K. K. *Physics of Semiconductor Devices*; John Wiley & Sons: Hoboken, 2006.

(7) (a) Ma, Y.; Shao, X.; Li, J.; Dong, B.; Hu, Z.; Zhou, Q.; Xu, H.; Zhao, X.; Fang, H.; Li, X.; Li, Z.; Wu, J.; Zhao, M.; Pennycook, S. J.; Sow, C. H.; Lee, C.; Zhong, Y. L.; Lu, J.; Ding, M.; Wang, K.; Li, Y.; Lu, J. Electrochemically exfoliated platinum dichalcogenide atomic layers for high-performance air-stable infrared photodetectors. *ACS Appl. Mater. Interfaces* **2021**, *13* (7), 8518−8527. (b) Alvarez, J.; Liao, M.; Koide, Y. Large deep-ultraviolet photocurrent in metal-semiconductor-metal structures fabricated on as-grown boron-doped diamond. *Appl. Phys. Lett.* **2005**, *87* (11), 113507. (c) Chen, X.; Liu, K.; Zhang, Z.; Wang, C.; Li, B.; Zhao, H.; Zhao, D.; Shen, D. Self-powered solar-blind photodetector with fast response based on Au/β-Ga_2O_3 nanowires array film Schottky junction. *ACS Appl. Mater. Interfaces* **2016**, *8* (6), 4185−4191. (d) Guo, D.; Su, Y.; Shi, H.; Li, P.; Zhao, N.; Ye, J.; Wang, S.; Liu, A.; Chen, Z.; Li, C.; Tang, W. Self-powered ultraviolet photodetector with superhigh photoresponsivity (3.05 A/W) based on the GaN/Sn: Ga_2O_3 pn junction. *ACS Nano* **2018**, *12* (12), 12827−12835. (e) Zhao, B.; Wang, F.; Chen, H.; Wang, Y.; Jiang, M.; Fang, X.; Zhao, D. Solar-blind avalanche photodetector based on single ZnO−Ga_2O_3 core−shell microwire. *Nano Lett.* **2015**, *15* (6), 3988−3993. (f) Zhang, H.; Liang, F.; Song, K.; Xing, C.; Wang, D.; Yu, H.; Huang, C.; Sun, Y.; Yang, L.; Zhao, X.; Sun, H.; Long, S. Demonstration of AlGaN/GaN-based ultraviolet phototransistor with a record high responsivity over 3.6×10^7 A/W. *Appl. Phys. Lett.* **2021**, *118* (24), 242105.

(8) (a) Yoshioka, S.; Hayashi, H.; Kuwabara, A.; Oba, F.; Matsunaga, K.; Tanaka, I. Structures and energetics of Ga_2O_3 polymorphs. *J. Phys.: Condens. Matter* **2007**, *19* (34), 346211. (b) Guo, D.; Guo, Q.; Chen, Z.; Wu, Z.; Li, P.; Tang, W. Review of Ga_2O_3-based optoelectronic devices. *Mater. Today Phys.* **2019**, *11*, 100157. (c) Geller, S. Crystal structure of β-Ga_2O_3. *J. Chem. Phys.* **1960**, *33* (3), 676−684. (d) Roy, R.; Hill, V.; Osborn, E. Polymorphism of Ga_2O_3 and the system Ga_2O_3—H_2O. *J. Am. Chem. Soc.* **1952**, *74* (3), 719−722. (e) Åhman, J.; Svensson, G.; Albertsson, J. A reinvestigation of β-gallium oxide. *Acta Crystallogr. C* **1996**, *52* (6), 1336−1338. (f) Zhang, J.; Shi, J.; Qi, D.-C.; Chen, L.; Zhang, K. H. Recent progress on the electronic structure, defect, and doping properties of Ga_2O_3. *APL Mater.* **2020**, *8* (2), No. 020906.

(9) (a) Yamaguchi, K. First principles study on electronic structure of β-Ga_2O_3. *Solid State Commun.* **2004**, *131* (12), 739−744. (b) Schubert, M.; Korlacki, R.; Knight, S.; Hofmann, T.; Schoche, S.; Darakchieva, V.; Janzen, E.; Monemar, B.; Gogova, D.; Thieu, Q.-T.; Togashi, R.; Murakami, H.; Kumagai, Y.; Goto, K.; Kuramata, A.; Yamakoshi, S.; Higashiwaki, M. Anisotropy, phonon modes, and free charge carrier parameters in monoclinic β-gallium oxide single crystals. *Phys. Rev. B* **2016**, *93* (12), 125209. (c) Guo, Z.; Verma, A.; Wu, X.; Sun, F.; Hickman, A.; Masui, T.; Kuramata, A.; Higashiwaki, M.; Jena, D.; Luo, T. Anisotropic thermal conductivity in single crystal β-gallium oxide. *Appl. Phys. Lett.* **2015**, *106* (11), 111909. (d) Jiang, P.; Qian, X.; Li, X.; Yang, R. Three-dimensional anisotropic thermal conductivity tensor of single crystalline β-Ga_2O_3. *Appl. Phys. Lett.* **2018**, *113* (23), 232105. (e) He, H.; Orlando, R.; Blanco, M. A.; Pandey, R.; Amzallag, E.; Baraille, I.; Rérat, M. First-principles study of the structural, electronic, and optical properties of Ga_2O_3 in its monoclinic and hexagonal phases. *Phys. Rev. B* **2006**, *74* (19), 195123. (f) Ueda, N.; Hosono, H.; Waseda, R.; Kawazoe, H. Anisotropy of electrical and optical properties in β-Ga_2O_3 single crystals. *Appl. Phys. Lett.* **1997**, *71* (7), 933−935.

(10) (a) Galazka, Z.; Uecker, R.; Irmscher, K.; Albrecht, M.; Klimm, D.; Pietsch, M.; Brützam, M.; Bertram, R.; Ganschow, S.; Fornari, R. Czochralski growth and characterization of β-Ga_2O_3 single crystals. *Cryst. Res. Technol.* **2010**, *45* (12), 1229−1236. (b) Kuramata, A.; Koshi, K.; Watanabe, S.; Yamaoka, Y.; Masui, T.; Yamakoshi, S. High-quality β-Ga_2O_3 single crystals grown by edge-defined film-fed growth. *Jpn. J. Appl. Phys.* **2016**, *55* (12), 1202A2. (c) Pratiyush, A. S.; Muazzam, U. U.; Kumar, S.; Vijayakumar, P.; Ganesamoorthy, S.; Subramanian, N.; Muralidharan, R.; Nath, D. N. Optical Float-Zone Grown Bulk β-Ga_2O_3-Based Linear MSM Array of UV-C Photo-detectors. *IEEE Photonic. Technol. L.* **2019**, *31* (12), 923−926. (d) Hoshikawa, K.; Ohba, E.; Kobayashi, T.; Yanagisawa, J.; Miyagawa, C.; Nakamura, Y. Growth of β-Ga_2O_3 single crystals using vertical Bridgman method in ambient air. *J. Cryst. Growth* **2016**, *447*, 36−41. (e) Zhang, T.; Li, Y.; Zhang, Y.; Feng, Q.; Ning, J.; Zhang, C.; Zhang, J.; Hao, Y. Effect of temperature on the structural and optical properties of Ga_2O_3 thin films grown on m-plane sapphire substrates by low-pressure MOCVD. *ECS J. Solid State Sc.* **2020**, *9* (6), No. 065009. (f) Wheeler, V. D.; Nepal, N.; Boris, D. R.; Qadri, S. B.; Nyakiti, L. O.; Lang, A.; Koehler, A.; Foster, G.; Walton, S. G.; Eddy, C. R.; Meyer, D. J. Phase control of crystalline Ga_2O_3 films by plasma-enhanced atomic layer deposition. *Chem. Mater.* **2020**, *32* (3), 1140−1152. (g) Ghosh, S.; Srivastava, H.; Rao, P.; Nand, M.; Tiwari, P.; Srivastava, A.; Jha, S.; Rai, S.; Singh, S.; Ganguli, T. Investigations on epitaxy and lattice distortion of sputter deposited β-Ga_2O_3 layers on GaN templates. *Semicond. Sci. Technol.* **2020**, *35* (8), No. 085024. (h) Yu, J.; Wang, Y.; Li, H.; Huang, Y.; Tang, W.; Wu, Z. Tailoring the solar-blind photoresponse characteristics of β-Ga2O3 epitaxial films through lattice mismatch and crystal orientation. *J. Phys. D: Appl. Phys.* **2020**, *53* (24), 24LT01. (i) Leach, J.; Udwary, K.; Rumsey, J.; Dodson, G.; Splawn, H.; Evans, K. Halide vapor phase epitaxial growth of β-Ga_2O_3 and α-Ga_2O_3 films. *APL Mater.* **2019**, *7* (2), No. 022504. (j) Lingaparthi, R.; Thieu, Q.; Koshi, K.; Wakimoto, D.; Sasaki, K.; Kuramata, A. Surface states on (001) oriented β-Ga_2O_3 epilayers, their origin, and their effect on the electrical properties of Schottky barrier diodes. *Appl. Phys. Lett.* **2020**, *116* (9), No. 092101. (k) Egyenes-Pörsök, F.; Gucmann, F.; Hušeková, K.; Dobročka, E.; Sobota, M.; Mikolášek, M.; Fröhlich, K.; Ťapajna, M. Growth of α-and β-Ga_2O_3 epitaxial layers on sapphire substrates using liquid-injection MOCVD. *Semicond. Sci. Technol.* **2020**, *35* (11), 115002. (l) Sun, H.; Li, K.-H.; Castanedo, C. T.; Okur, S.; Tompa, G. S.; Salagaj, T.; Lopatin, S.; Genovese, A.; Li, X. HCl flow-induced phase change of α-, β-, and ε-Ga_2O_3 films grown by MOCVD. *Cryst. Growth Des.* **2018**, *18* (4), 2370−2376. (m) Kalarickal, N. K.; Xia, Z.; McGlone, J.; Krishnamoorthy, S.; Moore, W.; Brenner, M.; Arehart, A. R.; Ringel, S. A.; Rajan, S. Mechanism of Si doping in plasma assisted MBE growth of β-Ga_2O_3. *Appl. Phys. Lett.* **2019**, *115* (15), 152106. (n) Mazzolini, P.; Bierwagen, O. Towards smooth (010) β-Ga_2O_3 films homoepitaxially grown by plasma assisted molecular beam epitaxy: The impact of substrate offcut and metal-to-oxygen flux ratio. *J. Phys. D: Appl. Phys.* **2020**, *53* (35), 354003. (o) Tak, B.; Dewan, S.; Goyal, A.; Pathak, R.; Gupta, V.; Kapoor, A.; Nagarajan, S.; Singh, R. Point defects induced work function modulation of β-Ga_2O_3. *Appl. Surf. Sci.* **2019**, *465*, 973−978. (p) Xu, C.; Liu, H.; Pan, X.; Ye, Z. Growth and characterization of Si-doped β-Ga_2O_3 films by pulsed laser deposition. *Opt. Mater.* **2020**, *108*, 110145. (q) Vanithakumari, S. C.; Nanda, K. K. A one-step method for the growth of Ga_2O_3-nanorod-based white-light-emitting phosphors. *Adv. Mater.* **2009**, *21* (35), 3581−3584.

(11) (a) Isberg, J.; Hammersberg, J.; Johansson, E.; Wikström, T.; Twitchen, D. J.; Whitehead, A. J.; Coe, S. E.; Scarsbrook, G. A. High carrier mobility in single-crystal plasma-deposited diamond. *Science* **2002**, *297* (5587), 1670−1672. (b) Aharonovich, I.; Greentree, A. D.; Prawer, S. Diamond photonics. *Nat. Photonics* **2011**, *5* (7), 397−405. (c) Balasubramanian, G.; Neumann, P.; Twitchen, D.; Markham, M.; Kolesov, R.; Mizuochi, N.; Isoya, J.; Achard, J.; Beck, J.; Tissler, J.; Jacques, V.; Hemmer, P. R.; Jelezko, F.; Wrachtrup, J. Ultralong spin coherence time in isotopically engineered diamond. *Nat. Mater.* **2009**, *8* (5), 383−387. (d) Qin, Z.; Wang, Z.; Kong, F.; Su, J.; Huang, Z.; Zhao, P.; Chen, S.; Zhang, Q.; Shi, F.; Du, J. In situ electron paramagnetic resonance spectroscopy using single nanodiamond sensors. *Nat. Commun.* **2023**, *14* (1), 6278. (e) Wang, P.; Yuan, Z.; Huang, P.; Rong, X.; Wang, M.; Xu, X.; Duan, C.; Ju, C.; Shi, F.; Du, J. High-resolution vector microwave magnetometry based on solid-state spins in diamond. *Nat. Commun.* **2015**, *6* (1), 6631. (f) Chen, Y.-C.; Lu, Y.-J.; Lin, C.-N.; Tian, Y.-Z.; Gao, C.-J.; Dong, L.; Shan, C.-X. Self-powered diamond/β-Ga_2O_3 photodetectors for solar-blind imaging. *J. Mater. Chem. C* **2018**, *6* (21), 5727−5732. (g) Zhou, A. F.; Velázquez, R.; Wang, X.; Feng, P. X. Nanoplasmonic 1D diamond UV photodetectors with high performance. *ACS Appl. Mater. Interfaces* **2019**, *11* (41), 38068−38074. (h) Perez, G.; Maréchal, A.; Chicot, G.; Lefranc, P.; Jeannin, P.-O.; Eon, D.; Rouger, N. Diamond semiconductor performances in power electronics applications. *Diamond Relat.*

Mater. **2020**, *110*, 108154. (i) Koizumi, S.; Watanabe, K.; Hasegawa, M.; Kanda, H. Ultraviolet emission from a diamond pn junction. *Science* **2001**, *292* (5523), 1899−1901. (j) Lohrmann, A.; Pezzagna, S.; Dobrinets, I.; Spinicelli, P.; Jacques, V.; Roch, J.-F.; Meijer, J.; Zaitsev, A. Diamond based light-emitting diode for visible single-photon emission at room temperature. *Appl. Phys. Lett.* **2011**, *99* (25), 251106.

(12) (a) Ma, Y.; Chen, J.; Wang, C. Growth of Diamond Thin Film and Creation of NV Centers. In *Applications and Use of Diamond*; IntechOpen, 2022. (b) Kanda, H.; Akaishi, M.; Yamaoka, S. New catalysts for diamond growth under high pressure and high temperature. *Appl. Phys. Lett.* **1994**, *65* (6), 784−786. (c) Abbaschian, R.; Zhu, H.; Clarke, C. High pressure−high temperature growth of diamond crystals using split sphere apparatus. *Diamond Relat. Mater.* **2005**, *14* (11−12), 1916−1919. (d) Sachan, R.; Bhaumik, A.; Pant, P.; Prater, J.; Narayan, J. Diamond film growth by HFCVD on Q-carbon seeded substrate. *Carbon* **2019**, *141*, 182−189. (e) Liu, Z.; Ao, J.-P.; Li, F.; Wang, W.; Wang, J.; Zhang, J.; Wang, H.-X. Fabrication of three dimensional diamond ultraviolet photodetector through down-top method. *Appl. Phys. Lett.* **2016**, *109* (15), 153507. (f) Garrison, B. J.; Dawnkaski, E. J.; Srivastava, D.; Brenner, D. W. Molecular dynamics simulations of dimer opening on a diamond {001}(2 × 1) surface. *Science* **1992**, *255* (5046), 835−838. (g) Arellano-Jimenez, M.; Alcantar-Peña, J.; Aguilar, J. O.; Yacaman, M.; Auciello, O. Polycrystalline diamond films produced by hot-filament chemical vapor deposition. *Microsc. Microanal.* **2017**, *23* (S1), 2272−2273. (h) Bakharev, P. V.; Huang, M.; Saxena, M.; Lee, S. W.; Joo, S. H.; Park, S. O; Dong, J.; Camacho-Mojica, D. C.; Jin, S.; Kwon, Y.; Biswal, M.; Ding, F.; Kwak, S. K.; Lee, Z.; Ruoff, R. S. Chemically induced transformation of chemical vapour deposition grown bilayer graphene into fluorinated single-layer diamond. *Nat. Nanotechnol.* **2020**, *15* (1), 59−66.

(13) (a) Nepal, N.; Li, J.; Nakarmi, M.; Lin, J.; Jiang, H. Temperature and compositional dependence of the energy band gap of AlGaN alloys. *Appl. Phys. Lett.* **2005**, *87* (24), 242104. (b) Schulz, H.; Thiemann, K. Crystal structure refinement of AlN and GaN. *Solid State Commun.* **1977**, *23* (11), 815−819.

(14) (a) Wu, Y.-F.; Kapolnek, D.; Ibbetson, J.P.; Parikh, P.; Keller, B.P.; Mishra, U.K. Very-high power density AlGaN/GaN HEMTs. *IEEE Trans. Electron Devices* **2001**, *48* (3), 586−590. (b) Ponce, F.; Bour, D. Nitride-based semiconductors for blue and green light-emitting devices. *Nature* **1997**, *386* (6623), 351−359. (c) Liu, Q.; Shi, J.; Wang, X.; Luo, X.; Guo, J.; Yang, Y.; Cheng, C.; Chen, F.; Deng, C.; He, L.; Fan, K.; Cui, Y.; Chen, K.; Gao, F.; Li, S. Enhanced photoresponse of single GaN microwire ultraviolet photodetectors by heteroepitaxial AlN coating layer. *Adv. Mater. Technol.* **2021**, *6* (8), 2100226. (d) Kuryatkov, V.; Chandolu, A.; Borisov, B.; Kipshidze, G.; Zhu, K.; Nikishin, S.; Temkin, H.; Holtz, M. Solar-blind ultraviolet photodetectors based on superlattices of AlN/AlGa(In)N. *Appl. Phys. Lett.* **2003**, *82* (9), 1323−1325. (e) Susilo, N.; Hagedorn, S.; Jaeger, D.; Miyake, H.; Zeimer, U.; Reich, C.; Neuschulz, B.; Sulmoni, L.; Guttmann, M.; Mehnke, F.; Kuhn, C.; Wernicke, T.; Weyers, M.; Kneissl, M. AlGaN-based deep UV LEDs grown on sputtered and high temperature annealed AlN/sapphire. *Appl. Phys. Lett.* **2018**, *112* (4), No. 041110.

(15) (a) Wang, Q.; Ge, Y.; Kuang, J.; Jiang, P.; Liu, W.; Cao, W. Effects of additives on the synthesis of spherical aluminum nitride granules by carbothermal reduction-nitridation process. *J. Alloys Compd.* **2017**, *696*, 220−225. (b) Hu, W.; Guo, L.; Guo, Y.; Wang, W. Growing AlN crystals on SiC seeds: Effects of growth temperature and seed orientation. *J. Cryst. Growth* **2020**, *541*, 125654. (c) Guerrero, R. M.; Garcia, J. R. V. Preparation of aluminum nitride thin films by CVD. *Mater. Manuf. Processes* **2000**, *15* (2), 259−267. (d) Chen, Y.; Zhang, Z.; Jiang, H.; Li, Z.; Miao, G.; Song, H. The optimized growth of AlN templates for back-illuminated AlGaN-based solar-blind ultraviolet photodetectors by MOCVD. *J. Mater. Chem. C* **2018**, *6* (18), 4936−4942. (e) Nikishin, S.; Faleev, N.; Antipov, V.; Francoeur, S.; Grave de Peralta, L.; Seryogin, G.; Temkin, H.; Prokofyeva, T.; Holtz, M.; Chu, S. High quality GaN grown on Si(111) by gas source molecular beam epitaxy with ammonia. *Appl. Phys. Lett.* **1999**, *75* (14), 2073−2075. (f) Yu, J.; Hao, Z.; Wang, J.; Deng, J.; Yu, W.; Wang, L.; Luo, Y.; Han, Y.; Sun, C.; Xiong, B.; Li, H. Study on AlN buffer layer for GaN on graphene/copper sheet grown by MBE at low growth temperature. *J. Alloys Compd.* **2019**, *783*, 633−642. (g) Ristoscu, C.; Ducu, C.; Socol, G.; Craciunoiu, F.; Mihailescu, I. Structural and optical characterization of AlN films grown by pulsed laser deposition. *Appl. Surf. Sci.* **2005**, *248* (1−4), 411−415. (h) Das, A.; Rath, M.; Nair, D. R.; Ramachandra Rao, M.S.; DasGupta, A. Realization of preferential (100) oriented AlN thin films on Mo coated Si substrate using reactive RF magnetron sputtering. *Appl. Surf. Sci.* **2021**, *550*, 149308. (i) Radwan, M.; Bahgat, M.; El-Geassy, A. Formation of aluminium nitride whiskers by direct nitridation. *J. Eur. Ceram. Soc.* **2006**, *26* (13), 2485−2488.

(16) (a) Kokubun, Y.; Miura, K.; Endo, F.; Nakagomi, S. Sol-gel prepared β-Ga_2O_3 thin films for ultraviolet photodetectors. *Appl. Phys. Lett.* **2007**, *90* (3), No. 031912. (b) Oshima, T.; Okuno, T.; Fujita, S. Ga_2O_3 thin film growth on c-plane sapphire substrates by molecular beam epitaxy for deep-ultraviolet photodetectors. *Jpn. J. Appl. Phys.* **2007**, *46* (11R), 7217. (c) Hu, G.; Shan, C.; Zhang, N.; Jiang, M.; Wang, S.; Shen, D. High gain Ga_2O_3 solar-blind photodetectors realized via a carrier multiplication process. *Opt. Express* **2015**, *23* (10), 13554−13561. (d) Zhang, D.; Zheng, W.; Lin, R.; Li, T.; Zhang, Z.; Huang, F. High quality β-Ga_2O_3 film grown with N_2O for high sensitivity solar-blind-ultraviolet photodetector with fast response speed. *J. Alloys Compd.* **2018**, *735*, 150−154. (e) Liu, X.; Guo, P.; Sheng, T.; Qian, L.; Zhang, W.; Li, Y. β-Ga_2O_3 thin films on sapphire pre-seeded by homo-self-templated buffer layer for solar-blind UV photodetector. *Opt. Mater.* **2016**, *51*, 203−207.

(17) (a) Wang, J.; Ji, X.; Yan, Z.; Qi, S.; liu, X.; Zhong, A.; Li, P. The role of oxygen vacancies in Ga_2O_3-based solar-blind photodetectors. *J. Alloys Compd.* **2024**, *970*, 172448. (b) Guo, D.; Wu, Z.; An, Y.; Guo, X.; Chu, X.; Sun, C.; Li, L.; Li, P.; Tang, W. Oxygen vacancy tuned Ohmic-Schottky conversion for enhanced performance in β-Ga_2O_3 solar-blind ultraviolet photodetectors. *Appl. Phys. Lett.* **2014**, *105* (2), No. 023507. (c) Zhou, C.; Liu, K.; Chen, X.; Feng, J.; Yang, J.; Zhang, Z.; Liu, L.; Xia, Y.; Shen, D. Performance improvement of amorphous Ga_2O_3 ultraviolet photodetector by annealing under oxygen atmosphere. *J. Alloys Compd.* **2020**, *840*, 155585. (d) Liang, H.; Cui, S.; Su, R.; Guan, P.; He, Y.; Yang, L.; Chen, L.; Zhang, Y.; Mei, Z.; Du, X. Flexible X-ray detectors based on amorphous Ga_2O_3 thin films. *ACS Photonics* **2019**, *6* (2), 351−359. (e) Oh, S.; Jung, Y.; Mastro, M. A.; Hite, J. K.; Eddy, C. R.; Kim, J. Development of solar-blind photodetectors based on Si-implanted β-Ga_2O_3. *Opt. Express* **2015**, *23* (22), 28300−28305. (f) Alema, F.; Hertog, B.; Ledyaev, O.; Volovik, D.; Thoma, G.; Miller, R.; Osinsky, A.; Mukhopadhyay, P.; Bakhshi, S.; Ali, H.; Schoenfeld, W. V. Solar blind photodetector based on epitaxial zinc doped Ga_2O_3 thin film. *Phys. Status Solidi A* **2017**, *214* (5), 1600688. (g) Guo, D.; Qin, X.; Lv, M.; Shi, H.; Su, Y.; Yao, G.; Wang, S.; Li, C.; Li, P.; Tang, W. Decrease of oxygen vacancy by Zn-doped for improving solar-blind photoelectric performance in β-Ga_2O_3 thin films. *Electron. Mater. Lett.* **2017**, *13*, 483−488.

(18) (a) Li, Y.; Tokizono, T.; Liao, M.; Zhong, M.; Koide, Y.; Yamada, I.; Delaunay, J. J. Efficient assembly of bridged β-Ga_2O_3 nanowires for solar-blind photodetection. *Adv. Funct. Mater.* **2010**, *20* (22), 3972−3978. (b) Zou, R.; Zhang, Z.; Liu, Q.; Hu, J.; Sang, L.; Liao, M.; Zhang, W. High detectivity solar-blind high-temperature deep-ultraviolet photodetector based on multi-layered (l00) facet-oriented β-Ga_2O_3 nanobelts. *Small* **2014**, *10* (9), 1848−1856. (c) Feng, W.; Wang, X.; Zhang, J.; Wang, L.; Zheng, W.; Hu, P.; Cao, W.; Yang, B. Synthesis of two-dimensional β-Ga_2O_3 nanosheets for high-performance solar blind photodetectors. *J. Mater. Chem. C* **2014**, *2* (17), 3254−3259. (d) Li, L.; Auer, E.; Liao, M.; Fang, X.; Zhai, T.; Gautam, U. K.; Lugstein, A.; Koide, Y.; Bando, Y.; Golberg, D. Deep-ultraviolet solar-blind photoconductivity of individual gallium oxide nanobelts. *Nanoscale* **2011**, *3* (3), 1120−1126. (e) Oh, S.; Kim, J.; Ren, F.; Pearton, S. J.; Kim, J. Quasi-two-dimensional β-gallium oxide solar-blind photodetectors with ultrahigh responsivity. *J. Mater. Chem. C* **2016**, *4* (39), 9245−9250. (f) Zhou, Y.; Zhang, Z.; Yang, X.; Liu, T.; He, G.; Lin, C.; Huang, W.-T.; Liu, H.; Wang, Y.; Wang, Y.; et al. Solar-Blind Photodetector Arrays Fabricated by Weaving Strategy. *ACS Nano* **2024**, *18* (10), 7610−7617. (g) Tian, W.; Zhi, C.; Zhai, T.; Chen, S.;

Wang, X.; Liao, M.; Golberg, D.; Bando, Y. In-doped Ga_2O_3 nanobelt based photodetector with high sensitivity and wide-range photo-response. *J. Mater. Chem.* **2012**, *22* (34), 17984−17991.

(19) (a) Cui, S.; Mei, Z.; Zhang, Y.; Liang, H.; Du, X. Room-temperature fabricated amorphous Ga_2O_3 high-response-speed solar-blind photodetector on rigid and flexible substrates. *Adv. Opt. Mater.* **2017**, *5* (19), 1700454. (b) Huang, L.; Feng, Q.; Han, G.; Li, F.; Li, X.; Fang, L.; Xing, X.; Zhang, J.; Hao, Y. Comparison study of β-Ga_2O_3 photodetectors grown on sapphire at different oxygen pressures. *IEEE Photonics J.* **2017**, *9* (4), 1−8. (c) Wang, J.; Ji, X.; Qi, S.; Li, Z.; Yan, Z.; Li, M.; Yan, X.; Zhong, A.; Lu, C.; Qi, X.; Li, P. Regulation of oxygen vacancies in nitrogen-doped Ga_2O_3 films for high-performance MSM solar-blind UV photodetectors. *J. Mater. Chem. C* **2023**, *11* (18), 6202−6211. (d) Qian, L.-X.; Wu, Z.-H.; Zhang, Y.-Y.; Lai, P.; Liu, X.-Z.; Li, Y.-R. Ultrahigh-responsivity, rapid-recovery, solar-blind photodetector based on highly nonstoichiometric amorphous gallium oxide. *ACS Photonics* **2017**, *4* (9), 2203−2211. (e) Lee, S. H.; Kim, S. B.; Moon, Y.-J.; Kim, S. M.; Jung, H. J.; Seo, M. S.; Lee, K. M.; Kim, S.-K.; Lee, S. W. High-responsivity deep-ultraviolet-selective photodetectors using ultra-thin gallium oxide films. *ACS Photonics* **2017**, *4* (11), 2937−2943. (f) Singh Pratiyush, A.; Krishnamoorthy, S.; Vishnu Solanke, S.; Xia, Z.; Muralidharan, R.; Rajan, S.; Nath, D. N. High responsivity in molecular beam epitaxy grown β-Ga_2O_3 metal semiconductor metal solar blind deep-UV photodetector. *Appl. Phys. Lett.* **2017**, *110* (22), 221107. (g) Labed, M.; Park, B.-I.; Kim, J.; Park, J. H.; Min, J. Y.; Hwang, H. J.; Kim, J.; Rim, Y. S. Ultrahigh Photoresponsivity of W/Graphene/β-Ga_2O_3 Schottky Barrier Deep Ultraviolet Photodiodes. *ACS Nano* **2024**, *18* (8), 6558−6569.

(20) (a) Yu, F.-P.; Ou, S.-L.; Wuu, D.-S. Pulsed laser deposition of gallium oxide films for high performance solar-blind photodetectors. *Opt. Mater. Express* **2015**, *5* (5), 1240−1249. (b) Shen, H.; Yin, Y.; Tian, K.; Baskaran, K.; Duan, L.; Zhao, X.; Tiwari, A. Growth and characterization of β-Ga_2O_3 thin films by sol-gel method for fast-response solar-blind ultraviolet photodetectors. *J. Alloys Compd.* **2018**, *766*, 601−608. (c) Chen, T.; Zhang, X.; Zhang, L.; Zeng, C.; Li, S.; Yang, A.; Hu, Y.; Li, B.; Jiang, M.; Huang, Z.; Li, Y.; Guo, G.; Fan, Y.; Shi, W.; Cai, Y.; Zeng, Z.; Zhang, B. High-Speed and Ultrasensitive Solar-Blind Ultraviolet Photodetectors Based on In Situ Grown β-Ga_2O_3 Single-Crystal Films. *ACS Appl. Mater. Interfaces* **2024**, *16*, 6068. (d) Arora, K.; Goel, N.; Kumar, M.; Kumar, M. Ultrahigh performance of self-powered β-Ga_2O_3 thin film solar-blind photodetector grown on cost-effective Si substrate using high-temperature seed layer. *ACS Photonics* **2018**, *5* (6), 2391−2401. (e) Feng, Z.; Huang, L.; Feng, Q.; Li, X.; Zhang, H.; Tang, W.; Zhang, J.; Hao, Y. Influence of annealing atmosphere on the performance of a β-Ga_2O_3 thin film and photodetector. *Optical Materials Express* **2018**, *8* (8), 2229−2237.

(21) (a) Zhang, C.; Liu, K.; Ai, Q.; Sun, X.; Chen, X.; Yang, J.; Zhu, Y.; Cheng, Z.; Li, B.; Liu, L.; Shen, D. High-performance fully transparent Ga_2O_3 solar-blind UV photodetector with the embedded indium−tin−oxide electrodes. *Mater. Today Phys.* **2023**, 33, 101034. (b) Oh, S.; Kim, C.-K.; Kim, J. High responsivity β-Ga_2O_3 metal−semiconductor−metal solar-blind photodetectors with ultraviolet transparent graphene electrodes. *ACS Photonics* **2018**, *5* (3), 1123−1128. (c) Kumar, N.; Arora, K.; Kumar, M. High performance, flexible and room temperature grown amorphous Ga_2O_3 solar-blind photodetector with amorphous indium-zinc-oxide transparent conducting electrodes. *J. Phys. D: Appl. Phys.* **2019**, *52* (33), 335103. (d) Wei, T.-C.; Tsai, D.-S.; Ravadgar, P.; Ke, J.-J.; Tsai, M.-L.; Lien, D.-H.; Huang, C.-Y.; Horng, R.-H.; He, J.-H. See-Through Ga_2O_3 Solar-Blind Photodetectors for Use in Harsh Environments. *IEEE J. Sel. Top. Quantum Electron.* **2014**, *20* (6), 112−117.

(22) (a) Oshima, T.; Okuno, T.; Arai, N.; Suzuki, N.; Ohira, S.; Fujita, S. Vertical solar-blind deep-ultraviolet Schottky photodetectors based on β-Ga_2O_3 substrates. *Appl. Phys. Express* **2008**, *1* (1), No. 011202. (b) Armstrong, A. M.; Crawford, M. H.; Jayawardena, A.; Ahyi, A.; Dhar, S. Role of self-trapped holes in the photoconductive gain of β-gallium oxide Schottky diodes. *J. Appl. Phys.* **2016**, *119* (10) DOI: 10.1063/1.4943261. (c) Peng, B.; Yuan, L.; Zhang, H.; Cheng, H.; Zhang, S.; Zhang, Y.; Zhang, Y.; Jia, R. Fast-response self-powered solar-blind photodetector based on Pt/β-Ga_2O_3 Schottky barrier diodes. *Optik* **2021**, *245*, 167715. (d) Wu, D.; Zhao, Z.; Lu, W.; Rogée, L.; Zeng, L.; Lin, P.; Shi, Z.; Tian, Y.; Li, X.; Tsang, Y. H. Highly sensitive solar-blind deep ultraviolet photodetector based on graphene/$PtSe_2$/β-Ga_2O_3 2D/3D Schottky junction with ultrafast speed. *Nano Res.* **2021**, *14*, 1973−1979. (e) Xu, Y.; Chen, X.; Zhang, Y.; Ren, F.; Gu, S.; Ye, J. Fast speed Ga_2O_3 solar-blind Schottky photodiodes with large sensitive area. *IEEE Electron Device Lett.* **2020**, *41* (7), 997−1000. (f) Yan, S.; Jiao, T.; Ding, Z.; Zhou, X.; Ji, X.; Dong, X.; Zhang, J.; Xin, Q.; Song, A. Ga_2O_3 Schottky Avalanche Solar-Blind Photodiode with High Responsivity and Photo-to-Dark Current Ratio. *Adv. Electron. Mater.* **2023**, *9* (11), 2300297. (g) Jiao, T.; Dang, X.; Chen, W.; Li, Z.; Diao, Z.; Chen, P.; Dong, X.; Zhang, Y.; Zhang, B. Self-powered Schottky barrier photodiodes based on homoepitaxial Ga_2O_3 film. *Mater. Lett.* **2023**, *349*, 134847. (h) Alema, F.; Hertog, B.; Mukhopadhyay, P.; Zhang, Y.; Mauze, A.; Osinsky, A.; Schoenfeld, W. V.; Speck, J. S.; Vogt, T. Solar blind Schottky photodiode based on an MOCVD-grown homoepitaxial β-Ga_2O_3 thin film. *APL Mater.* **2019**, *7* (2), No. 022527. (i) Suzuki, R.; Nakagomi, S.; Kokubun, Y.; Arai, N.; Ohira, S. Enhancement of responsivity in solar-blind β-Ga_2O_3 photodiodes with a Au Schottky contact fabricated on single crystal substrates by annealing. *Appl. Phys. Lett.* **2009**, *94* (22), 222102. (j) Suzuki, R.; Nakagomi, S.; Kokubun, Y. Solar-blind photodiodes composed of a Au Schottky contact and a β-Ga_2O_3 single crystal with a high resistivity cap layer. *Appl. Phys. Lett.* **2011**, *98* (13), 131114. (k) Yang, L.-L.; Liu, Z.; Li, S.; Zhang, M.-L.; Xi, Z.-Y.; Xu, Q.; Yan, S.-H.; Guo, Y.-F.; Tang, W.-H. Enhancing Carrier Transport and Injection of Ga_2O_3 Deep-Ultraviolet Schottky Photodiode by Introducing Impurity Energy Level. *IEEE Electron Device Lett.* **2024**.453420

(23) (a) Xie, C.; Lu, X. T.; Tong, X. W.; Zhang, Z. X.; Liang, F. X.; Liang, L.; Luo, L. B.; Wu, Y. C. Recent progress in solar-blind deep-ultraviolet photodetectors based on inorganic ultrawide bandgap semiconductors. *Adv. Funct. Mater.* **2019**, *29* (9), 1806006. (b) Kaur, D.; Kumar, M. A strategic review on gallium oxide based deep-ultraviolet photodetectors: recent progress and future prospects. *Adv. Opt. Mater.* **2021**, *9* (9), 2002160. (c) Chen, X.; Ren, F.; Gu, S.; Ye, J. Review of gallium-oxide-based solar-blind ultraviolet photodetectors. *Photonics Res.* **2019**, *7* (4), 381−415. (d) Xu, J.; Zheng, W.; Huang, F. Gallium oxide solar-blind ultraviolet photodetectors: a review. *J. Mater. Chem. C* **2019**, *7* (29), 8753−8770.

(24) (a) Yamaga, M.; Víllora, E. G.; Shimamura, K.; Ichinose, N.; Honda, M. Donor structure and electric transport mechanism in β-Ga_2O_3. *Phys. Rev. B* **2003**, *68* (15), 155207. (b) Varley, J. B.; Janotti, A.; Franchini, C.; Van de Walle, C. G. Role of self-trapping in luminescence and p-type conductivity of wide-band-gap oxides. *Phys. Rev. B* **2012**, *85* (8), No. 081109.

(25) (a) Nakagomi, S.; Momo, T.; Takahashi, S.; Kokubun, Y. Deep ultraviolet photodiodes based on β-Ga_2O_3/SiC heterojunction. *Appl. Phys. Lett.* **2013**, *103* (7), No. 072105. (b) Kong, W.-Y.; Wu, G.-A.; Wang, K.-Y.; Zhang, T.-F.; Zou, Y.-F.; Wang, D.-D.; Luo, L.-B. Graphene-β-Ga_2O_3 heterojunction for highly sensitive deep UV photodetector application. *Adv. Mater.* **2016**, *28* (48), 10725−10731. (c) Lin, R.; Zheng, W.; Zhang, D.; Zhang, Z.; Liao, Q.; Yang, L.; Huang, F. High-performance graphene/β-Ga_2O_3 heterojunction deep-ultraviolet photodetector with hot-electron excited carrier multiplication. *ACS Appl. Mater. Interfaces* **2018**, *10* (26), 22419−22426. (d) Ai, M.; Guo, D.; Qu, Y.; Cui, W.; Wu, Z.; Li, P.; Li, L.; Tang, W. Fast-response solar-blind ultraviolet photodetector with a graphene/β-Ga_2O_3/graphene hybrid structure. *J. Alloys Compd.* **2017**, *692*, 634−638. (e) Higashiwaki, M.; Sasaki, K.; Murakami, H.; Kumagai, Y.; Koukitu, A.; Kuramata, A.; Masui, T.; Yamakoshi, S. β-Ga_2O_3/p-Type 4H-SiC Heterojunction Diodes and Applications to Deep-UV Photodiodes. *Semicond. Sci. Technol.* **2016**, *31*, No. 034001. (f) Guo, X.; Hao, N.; Guo, D.; Wu, Z.; An, Y.; Chu, X.; Li, L.; Li, P.; Lei, M.; Tang, W. β-Ga_2O_3/p-Si heterojunction solar-blind ultraviolet photodetector with enhanced photoelectric responsivity. *J. Alloys Compd.* **2016**, *660*, 136−140. (g) Guo, D Y; Shi, H Z; Qian, Y P; Lv, M; Li, P G; Su, Y L; Liu, Q; Chen, K; Wang, S L; Cui, C; Li, C R; Tang, W H Fabrication of β-Ga_2O_3/ZnO heterojunction for solar-blind deep ultraviolet photo-

detection. *Semicond. Sci. Technol.* **2017**, *32* (3), 03LT01. (h) He, T.; Zhao, Y.; Zhang, X.; Lin, W.; Fu, K.; Sun, C.; Shi, F.; Ding, X.; Yu, G.; Zhang, K.; Lu, S.; Zhang, X.; Zhang, B. Solar-blind ultraviolet photodetector based on graphene/vertical Ga_2O_3 nanowire array heterojunction. *Nanophotonics* **2018**, *7* (9), 1557−1562. (i) Kalita, G.; Mahyavanshi, R. D.; Desai, P.; Ranade, A. K.; Kondo, M.; Dewa, T.; Tanemura, M. Photovoltaic Action in Graphene−Ga_2O_3 Heterojunction with Deep-Ultraviolet Irradiation. *Phys. Status Solidi RRL* **2018**, *12* (8), 1800198. (j) Li, K.-H.; Alfaraj, N.; Kang, C. H.; Braic, L.; Hedhili, M. N.; Guo, Z.; Ng, T. K.; Ooi, B. S. Deep-ultraviolet photodetection using single-crystalline β-Ga_2O_3/NiO heterojunctions. *ACS Appl. Mater. Interfaces* **2019**, *11* (38), 35095−35104. (k) Bae, H.; Charnas, A.; Sun, X.; Noh, J.; Si, M.; Chung, W.; Qiu, G.; Lyu, X.; Alghamdi, S.; Wang, H.; Zemlyanov, D.; Ye, P. D. Solar-blind UV photodetector based on atomic layer-deposited Cu_2O and nanomembrane β-Ga_2O_3 pn oxide heterojunction. *ACS Omega* **2019**, *4* (24), 20756−20761. (l) Nakagomi, S.; Sakai, T.; Kikuchi, K.; Kokubun, Y. β-Ga_2O_3/p-type 4H-SiC heterojunction diodes and applications to deep-UV photodiodes. *Phys. Status Solidi A* **2019**, *216* (5), 1700796. (m) Mahmoud, W. E. Solar blind avalanche photodetector based on the cation exchange growth of β-Ga_2O_3/SnO_2 bilayer heterostructure thin film. *Sol. Energy Mater. Sol. Cells* **2016**, *152*, 65−72.

(26) (a) Chen, M.; Ma, J.; Li, P.; Xu, H.; Liu, Y. Zero-biased deep ultraviolet photodetectors based on graphene/cleaved (100) Ga_2O_3 heterojunction. *Opt. Express* **2019**, *27* (6), 8717−8726. (b) Li, P.; Shi, H.; Chen, K.; Guo, D.; Cui, W.; Zhi, Y.; Wang, S.; Wu, Z.; Chen, Z.; Tang, W. Construction of GaN/Ga_2O_3 p−n junction for an extremely high responsivity self-powered UV photodetector. *J. Mater. Chem. C* **2017**, *5* (40), 10562−10570. (c) Wang, Y.; Li, L.; Wang, H.; Su, L.; Chen, H.; Bian, W.; Ma, J.; Li, B.; Liu, Z.; Shen, A. An ultrahigh responsivity self-powered solar-blind photodetector based on a centimeter-sized β-Ga_2O_3/polyaniline heterojunction. *Nanoscale* **2020**, *12* (3), 1406−1413. (d) Zeng, G.; Zhang, M.-R.; Chen, Y.-C.; Li, X.-X.; Chen, D.-B.; Shi, C.-Y.; Zhao, X.-F.; Chen, N.; Wang, T.-Y.; Zhang, D. W.; Lu, H.-L. A solar-blind photodetector with ultrahigh rectification ratio and photoresponsivity based on the $MoTe_2$/Ta: β-Ga_2O_3 pn junction. *Mater. Today Phys.* **2023**, *33*, 101042. (e) Guo, D.; Liu, H.; Li, P.; Wu, Z.; Wang, S.; Cui, C.; Li, C.; Tang, W. Zero-power-consumption solar-blind photodetector based on β-Ga_2O_3/NSTO heterojunction. *ACS Appl. Mater. Interfaces* **2017**, *9* (2), 1619−1628. (f) Chen, R.; Wang, D.; Feng, B.; Zhu, H.; Han, X.; Ma, J.; Xiao, H.; Luan, C. High responsivity self-powered DUV photodetectors based on β-Ga_2O_3/GaN heterogeneous PN junctions. *Vacuum* **2023**, *215*, 112332. (g) Zhao, B.; Wang, F.; Chen, H.; Zheng, L.; Su, L.; Zhao, D.; Fang, X. An ultrahigh responsivity (9.7 mA W^{-1}) self-powered solar-blind photodetector based on individual ZnO−Ga_2O_3 heterostructures. *Adv. Funct. Mater.* **2017**, *27* (17), 1700264.

(27) (a) Chen, W.; Xu, X.; Li, M.; Kuang, S.; Zhang, K. H.; Cheng, Q. A fast self-powered solar-blind ultraviolet photodetector realized by Ga_2O_3/GaN PIN heterojunction with a fully depleted active region. *Adv. Opt. Mater.* **2023**, *11* (8), 2202847. (b) Kan, H.; Zheng, W.; Fu, C.; Lin, R.; Luo, J.; Huang, F. Ultrawide band gap oxide nanodots (E_g > 4.8 eV) for a high-performance deep ultraviolet photovoltaic detector. *ACS Appl. Mater. Interfaces* **2020**, *12* (5), 6030−6036. (c) Chen, R.; Wang, D.; Han, X.; Feng, B.; Zhu, H.; Luan, C.; Ma, J.; Xiao, H. Self-powered deep ultraviolet PIN photodetectors with excellent response performance based on Ga_2O_3 epitaxial films grown on p-GaN. *Appl. Phys. Lett.* **2023**, *123* (8), No. 082101.

(28) (a) Yu, J.; Boyd, I. UV detection for excimer lamps using CVD diamond in various gaseous atmospheres. *Diamond Relat. Mater.* **2007**, *16* (3), 494−497. (b) Liao, M.; Koide, Y. High-performance metal-semiconductor-metal deep-ultraviolet photodetectors based on homoepitaxial diamond thin film. *Appl. Phys. Lett.* **2006**, *89* (11), 113509. (c) Lin, C. N.; Lu, Y. J.; Yang, X.; Tian, Y. Z.; Gao, C. J.; Sun, J. L.; Dong, L.; Zhong, F.; Hu, W. D.; Shan, C. X. Diamond-based all-carbon photodetectors for solar-blind imaging. *Adv. Opt. Mater.* **2018**, *6* (15), 1800068. (d) Qiu, M.; Jia, Z.; Yang, M.; Li, M.; Shen, Y.; Liu, C.; Nishimura, K.; Jiang, N.; Wang, B.; Lin, C.-T.; Yuan, Q. High-performance single crystal diamond pixel photodetector with nanosecond rise time for solar-blind imaging. *Diamond Relat. Mater.* **2024**, *144*, 110996. (e) Gorokhov, E.; Magunov, A.; Feshchenko, V.; Altukhov, A. Solar-blind UV flame detector based on natural diamond. *Instrum. Exp. Tech.* **2008**, *51* (2), 280−283.

(29) (a) Alemanno, E.; Martino, M.; Caricato, A. P.; Corrado, M.; Pinto, C.; Spagnolo, S.; Chiodini, G.; Perrino, R.; Fiore, G. Laser induced nano-graphite electrical contacts on synthetic polycrystalline CVD diamond for nuclear radiation detection. *Diamond Relat. Mater.* **2013**, *38*, 32−35. (b) Liu, K.; Dai, B.; Ralchenko, V.; Xia, Y.; Quan, B.; Zhao, J.; Shu, G.; Sun, M.; Gao, G.; Yang, L.; Lei, P.; Han, J.; Zhu, J. Single crystal diamond UV detector with a groove-shaped electrode structure and enhanced sensitivity. *Sens. Actuators A* **2017**, *259*, 121−126. (c) Caylar, B.; Pomorski, M.; Bergonzo, P. Laser-processed three dimensional graphitic electrodes for diamond radiation detectors. *Appl. Phys. Lett.* **2013**, *103* (4), No. 043504. (d) Forneris, J.; Battiato, A.; Gatto Monticone, D.; Picollo, F.; Amato, G.; Boarino, L.; Brida, G.; Degiovanni, I.P.; Enrico, E.; Genovese, M.; Moreva, E.; Traina, P.; Verona, C.; Verona Rinati, G.; Olivero, P. Electroluminescence from a diamond device with ion-beam-micromachined buried graphitic electrodes. *Nucl. Instrum. Methods Phys. Res., Sect. B* **2015**, *348*, 187−190.

(30) (a) Binari, S.; Marchywka, M.; Koolbeck, D.; Dietrich, H.; Moses, D. Diamond metal-semiconductor-metal ultraviolet photodetectors. *Diamond Relat. Mater.* **1993**, *2* (5−7), 1020−1023. (b) Wang, L.; Chen, X.; Wu, G.; Guo, W.; Wang, Y.; Cao, S.; Shang, K.; Han, W. Study on trapping center and trapping effect in MSM ultraviolet photo-detector on microcrystalline diamond film. *Phys. Status Solidi A* **2010**, *207* (2), 468−473. (c) Liao, M.; Alvarez, J.; Imura, M.; Koide, Y. Submicron metal-semiconductor-metal diamond photodiodes toward improving the responsivity. *Appl. Phys. Lett.* **2007**, *91* (16), 163510. (d) Salvatori, S.; Della Scala, A.; Rossi, M.; Conte, G. Optimised contact-structures for metal−diamond−metal UV-detectors. *Diamond Relat. Mater.* **2002**, *11* (3−6), 458−462.

(31) (a) Chang, X.; Wang, Y.-F.; Abbasi, H. N.; Wang, R.; Liu, Z.; Wang, J.; Song, W.; Chen, G.; Zhang, M.; Wang, W.; Wang, K.; Wang, H.-X. Pd nanoparticle size effects in localized surface plasmon-enhanced diamond photodetectors. *Opt. Mater.* **2020**, *107*, 110031. (b) Shi, X.; Yang, Z.; Yin, S.; Zeng, H. Al plasmon-enhanced diamond solar-blind UV photodetector by coupling of plasmon and excitons. *Mater. Technol.* **2016**, *31* (9), 544−547. (c) Chang, X.; Wang, Y.-F.; Zhang, X.; Liu, Z.; Fu, J.; Zhao, D.; Fan, S.; Bu, R.; Zhang, J.; Wang, W.; Wang, H.-X. Enhanced ultraviolet absorption in diamond surface via localized surface plasmon resonance in palladium nanoparticles. *Appl. Surf. Sci.* **2019**, *464*, 455−457.

(32) (a) Lin, C.-N.; Zhang, Z.-F.; Lu, Y.-J.; Yang, X.; Zhang, Y.; Li, X.; Zang, J.-H.; Pang, X.-C.; Dong, L.; Shan, C.-X. High performance diamond-based solar-blind photodetectors enabled by Schottky barrier modulation. *Carbon* **2022**, *200*, 510−516. (b) Ge, L.; Li, B.; Li, G.; Wang, X.; Cheong, K. Y.; Peng, Y.; Han, J.; Li, S.; Cui, Y.; Zhong, Y.; Cui, P.; Wang, D.; Xu, M.; Xu, X. High-Performance Diamond Phototransistor with Gate Controllable Gain and Speed. *J. Phys. Chem. Lett.* **2023**, *14* (2), 592−597.

(33) (a) Whitfield, M. D.; McKeag, R. D.; Pang, L. Y.; Chan, S. S.; Jackman, R. B. Thin film diamond UV photodetectors: Photodiodes compared with photoconductive devices for highly selective wavelength response. *Diamond Relat. Mater.* **1996**, *5* (6−8), 829−834. (b) Whitfield, M. D.; Chan, S. S.; Jackman, R. B. Thin film diamond photodiode for ultraviolet light detection. *Appl. Phys. Lett.* **1996**, *68* (3), 290−292. (c) Koide, Y. Metal−diamond semiconductor interface and photodiode application. *Appl. Surf. Sci.* **2008**, *254* (19), 6268−6272. (d) Koide, Y.; Liao, M.; Alvarez, J. Thermally stable solar-blind diamond UV photodetector. *Diamond Relat. Mater.* **2006**, *15* (11−12), 1962−1966. (e) Liao, M.; Koide, Y.; Alvarez, J. Photovoltaic Schottky ultraviolet detectors fabricated on boron-doped homoepitaxial diamond layer. *Appl. Phys. Lett.* **2006**, *88* (3), No. 033504. (f) Li, F.; Li, Y.; Fan, D.; Wang, H. Self-powered diamond ultraviolet photodetector with a transparent Ag nanowire electrode. *Nanotechnology* **2019**, *30* (32), 325204. (g) Girolami, M.; Serpente, V.; Mastellone, M.; Tardocchi, M.; Rebai, M.; Xiu, Q.; Liu, J.; Sun, Z.; Zhao, Y.; Valentini,

V.; Trucchi, D. M. Self-powered solar-blind ultrafast UV-C diamond detectors with asymmetric Schottky contacts. *Carbon* **2022**, *189*, 27−36. (h) Liu, B.; Liu, K.; Zhang, S.; Ralchenko, V. G.; Zhang, X.; Xue, J.; Wen, D.; Qiao, P.; Zhao, J.; Dai, B.; Yang, L.; Han, J.; Zhu, J. Self-powered solar-blind UV detectors based on O-terminated vertical diamond Schottky diode with low dark current, high detectivity, and high signal-to-noise ratio. *ACS Appl. Electron. Mater.* **2022**, *4* (12), 5996−6003.

(34) (a) Koizumi, S.; Kamo, M.; Sato, Y.; Ozaki, H.; Inuzuka, T. Growth and characterization of phosphorous doped {111} homoepitaxial diamond thin films. *Appl. Phys. Lett.* **1997**, *71* (8), 1065−1067. (b) Gheeraert, E.; Casanova, N.; Tajani, A.; Deneuville, A.; Bustarret, E.; Garrido, J.; Nebel, C.; Stutzmann, M. n-Type doping of diamond by sulfur and phosphorus. *Diamond Relat. Mater.* **2002**, *11* (3−6), 289−295. (c) Barber, G. D.; Yarbrough, W. A. Growth Rate of Diamond on Polycrystalline< 110> Diamond Substrates from Carbon Disulfide in Hydrogen by Hot-Filament-Assisted Chemical Vapor Deposition. *J. Am. Ceram. Soc.* **1997**, *80* (6), 1560−1566. (d) BenMoussa, A.; Hochedez, J.F.; Schuhle, U.; Schmutz, W.; Haenen, K.; Stockman, Y.; Soltani, A.; Scholze, F.; Kroth, U.; Mortet, V.; Theissen, A.; Laubis, C.; Richter, M.; Koller, S.; Defise, J.-M.; Koizumi, S. Diamond detectors for LYRA, the solar VUV radiometer on board PROBA2. *Diamond Relat. Mater.* **2006**, *15* (4−8), 802−806. (e) BenMoussa, A; Schuhle, U; Scholze, F; Kroth, U; Haenen, K; Saito, T; Campos, J; Koizumi, S; Laubis, C; Richter, M; Mortet, V; Theissen, A; Hochedez, J F Radiometric characteristics of new diamond PIN photodiodes. *Meas. Sci. Technol.* **2006**, *17* (4), 913.

(35) (a) Wan, Y.; Gao, S.; Li, L.; Zhang, J.; Fan, H.; Jiao, S.; Wang, J.; Yu, Q.; Wang, D. Efficient UV photodetector based on heterojunction of n-ZnO nanorods/p-diamond film. *J. Mater. Sci.: Mater. Electron.* **2017**, *28*, 11172−11177. (b) Su, R.; Liu, Z.; Chang, X.; Liang, Y.; Chen, G.; Yan, X.; Li, F.; Shao, G.; Pan, J.; Abbasi, H. N.; Wang, H. Characterization of UV photodetector based on ZnO/diamond film. *Opt. Express* **2019**, *27* (25), 36750−36756. (c) Liu, Z.; Li, F.; Li, S.; Hu, C.; Wang, W.; Wang, F.; Lin, F.; Wang, H. Fabrication of UV photodetector on TiO_2/diamond film. *Sci. Rep.* **2015**, *5* (1), 14420. (d) Liu, Z.; Ao, J.-P.; Li, F.; Wang, W.; Wang, J.; Zhang, J.; Wang, H.-X. Photoelectrical characteristics of ultra thin TiO_2/diamond photodetector. *Mater. Lett.* **2017**, *188*, 52−54. (e) Wei, M.; Yao, K.; Liu, Y.; Yang, C.; Zang, X.; Lin, L. A solar-blind UV detector based on graphene-microcrystalline diamond heterojunctions. *Small* **2017**, *13* (34), 1701328. (f) Li, F.; Bao, H.; Li, Y.; Ma, F.; Wang, H. Laser induced diamond/graphite structure for all-carbon deep-ultraviolet photodetector. *Appl. Surf. Sci.* **2023**, *636*, 157818.

(36) (a) Lebedev, V.; Cimalla, I.; Kaiser, U.; Ambacher, O. Gap state absorption in AlGaN photoconductors and solar-blind photodetectors. *Phys. Status Solidi C* **2004**, *1* (2), 233−237. (b) Cherkashinin, G.; Lebedev, V.; Wagner, R.; Cimalla, I.; Ambacher, O. The performance of AlGaN solar blind UV photodetectors: responsivity and decay time. *Phys. Status Solidi B* **2006**, *243* (7), 1713−1717. (c) Nikishin, S.; Borisov, B.; Pandikunta, M.; Dahal, R.; Lin, J.; Jiang, H.; Harris, H.; Holtz, M. High quality AlN for deep UV photodetectors. *Appl. Phys. Lett.* **2009**, *95* (5), No. 054101. (d) Xie, F.; Lu, H.; Chen, D.; Ji, X.; Yan, F.; Zhang, R.; Zheng, Y.; Li, L.; Zhou, J. Ultra-low dark current AlGaN-based solar-blind metal−semiconductor−metal photodetectors for high-temperature applications. *IEEE Sens. J.* **2012**, *12* (6), 2086−2090. (e) Bao, G.; Li, D.; Sun, X.; Jiang, M.; Li, Z.; Song, H.; Jiang, H.; Chen, Y.; Miao, G.; Zhang, Z. Enhanced spectral response of an AlGaN-based solar-blind ultraviolet photodetector with Al nanoparticles. *Opt. Express* **2014**, *22* (20), 24286−24293. (f) Chen, C.-H.; Chang, S.-J.; Wu, M.-H.; Tsai, S.-Y.; Chien, H.-J. AlGaN metal−semiconductor−metal photodetectors with low-temperature AlN cap layer and recessed electrodes. *Jpn. J. Appl. Phys.* **2010**, *49* (4S), 04DG05. (g) Fang, T.; Jiang, K.; Wang, B.; Zhang, S.; Xie, Z.; Ben, J.; Zhang, Z.; Chen, Y.; Jia, Y.; Liu, M.; et al. The Insertion of an AlN Spacer between the Barrier and the Channel Layer for a Polarization-Enhanced AlGaN-Based Solar-Blind Ultraviolet Detector. *ACS Appl. Electron. Mater.* **2024**, *6* (4), 2490−2499.

(37) (a) Zhang, H.; Liang, F.; Song, K.; Xing, C.; Wang, D.; Yu, H.; Huang, C.; Sun, Y.; Yang, L.; Zhao, X.; Sun, H.; Long, S. Demonstration of AlGaN/GaN-based ultraviolet phototransistor with a record high responsivity over 3.6× 10^7 A/W. *Appl. Phys. Lett.* **2021**, *118* (24), 242105. (b) Lu, J.; Lv, Z.; Jiang, H. AlGaN solar-blind phototransistor capable of directly detecting sub-fW signals: self-depletion and photorecovery of full-channel 2DEG enabled by a quasi-pseudomorphic structure. *Photonics Res.* **2023**, *11* (7), 1217−1226. (c) Wang, H.; Feng, M.; Zhong, Y.; Chen, X.; Gao, H.; Yilmaz, E.; Sun, Q.; Yang, H. Ultrahigh-Responsivity Ultraviolet Photodetectors Based on AlGaN/GaN Double-Channel High-Electron-Mobility Transistors. *ACS Photonics* **2024**, *11* (1), 180−186. (d) Yang, L.; Zhang, H.; Sun, Y.; Hu, K.; Xing, Z.; Liang, K.; Fang, S.; Wang, D.; Yu, H.; Kang, Y.; Sun, H. Temperature-dependent photodetection behavior of AlGaN/GaN-based ultraviolet phototransistors. *Appl. Phys. Lett.* **2022**, *120* (9), No. 091103.

(38) (a) Osinsky, A.; Gangopadhyay, S.; Lim, B.; Anwar, M.; Khan, M. A.; Kuksenkov, D.; Temkin, H. Schottky barrier photodetectors based on AlGaN. *Appl. Phys. Lett.* **1998**, *72* (6), 742−744. (b) Adivarahan, V.; Simin, G.; Tamulaitis, G.; Srinivasan, R.; Yang, J.; Khan, M. A.; Shur, M.; Gaska, R. Indium−silicon co-doping of high-aluminum-content AlGaN for solar blind photodetectors. *Appl. Phys. Lett.* **2001**, *79* (12), 1903−1905. (c) Biyikli, N.; Kimukin, I.; Kartaloglu, T.; Aytur, O.; Ozbay, E. High-speed solar-blind photodetectors with indium-tin-oxide Schottky contacts. *Appl. Phys. Lett.* **2003**, *82* (14), 2344−2346. (d) Gu, Y.; Guo, J.; Ye, B.; Yang, X.; Xie, F.; Qian, W.; Zhang, X.; Lu, N.; Liu, Y.; Yang, G. Self-powered AlGaN-based MSM solar-blind ultraviolet photodetectors with high Al-content AlxGa1-xN/AlyGa1-yN asymmetrical heterostructure. *Appl. Phys. Lett.* **2023**, *123* (23), 232103. (e) Guo, C.; Zhang, J.; Xia, S.; Deng, L.; Liu, K.; Yang, Z.; Cheng, B.; Sarkar, B.; Guo, W.; Ye, J. Self-powered MSM solar-blind AlGaN photodetector realized by in-plane polarization modulation. *Opt. Lett.* **2023**, *48* (18), 4769−4772.

(39) (a) Parish, G.; Keller, S.; Kozodoy, P.; Ibbetson, J.; Marchand, H.; Fini, P.; Fleischer, S.; DenBaars, S.; Mishra, U.; Tarsa, E. High-performance (Al, Ga) N-based solar-blind ultraviolet p−i−n detectors on laterally epitaxially overgrown GaN. *Appl. Phys. Lett.* **1999**, *75* (2), 247−249. (b) McClintock, R.; Yasan, A.; Mayes, K.; Shiell, D.; Darvish, S.; Kung, P.; Razeghi, M. High quantum efficiency AlGaN solar-blind pin photodiodes. *Appl. Phys. Lett.* **2004**, *84* (8), 1248−1250. (c) Cicek, E.; McClintock, R.; Cho, C.; Rahnema, B.; Razeghi, M. AlxGa1-xN-based back-illuminated solar-blind photodetectors with external quantum efficiency of 89%. *Appl. Phys. Lett.* **2013**, *103* (19), 191108. (d) Huang, C.; Liang, F.; Yu, H.; Tian, M.; Zhang, H.; Ng, T. K.; Ooi, B. S.; Sun, H. Boosted ultraviolet photodetection of AlGaN quantum-disk nanowires via rational surface passivation. *J. Phys. D: Appl. Phys.* **2022**, *55* (12), 125101. (e) Muhtadi, S.; Hwang, S. M.; Coleman, A. L.; Lunev, A.; Asif, F.; Chava, V.; Chandrashekhar, M.; Khan, A. High-speed solar-blind UV photodetectors using high-Al content $Al_{0.64}Ga_{0.36}N/Al_{0.34}Ga_{0.66}N$ multiple quantum wells. *Appl. Phys. Express* **2017**, *10* (1), No. 011004.